Depth Dependant Dielectric Constant and Second Order Response at Aqueous Interfaces

by

Peter Yang
B.Sc., University of Victoria, 2023

A Thesis Submitted in Partial Fulfillment of the
Requirements for the Degree of

MASTER OF SCIENCE

in the Department of Chemistry

Depth Dependant Dielectric Constant and Second Order Response at Aqueous Interfaces

by

Peter Yang
B.Sc., University of Victoria, 2023

Supervisory committee

Dr. Dennis K. Hore, Supervisor
(Department of Chemistry, Department of Computer Science)

Dr. Peter Loock, Departmental Member
(Department of Chemistry)

ABSTRACT

Aqueous interfacial environments have unique properties as a result of their inherent anisotropy; however, analysis of interfacial regions remains challenging. Sum-frequency generation measurements can be used for their study, although determining the linear-optical properties, and the molecular electronic structure required for quantitative analysis remains difficult. From classical molecular dynamics simulations we found the orientation distribution to be invariant with increasing surface number density; we can also therefore expect the ordering of cyanophenol to be a result of interfacial water. We describe the necessity of depth dependence to the sum-frequency response by using interfacial structure from classical molecular dynamics. By exploiting symmetry, we can derive linear relationships between elements of the $\chi^{(2)}$ tensor which shed light on future sum-frequency based orientational measurements. The range of possible values for the interfacial hyperpolarizability ratio has been significantly narrowed with the aid of classical molecular dynamics simulations. We also propose a technique for experimentally measuring the hyperpolarizability ratio that has been derived by exploiting the polarisation null angle method. By using Raman spectra derived from interfacial and bulk-phase *ab initio* simulations we conclude there to be little difference in the hyperpolarizability ratio in the interfacial or bulk environments; by comparing with experimental Raman measurements we also report the existence of asymmetric broadening in the C–N mode.

Contents

List of Figures

List of Tables

List of Symbols and Definitions

symbol	definition
SFG	sum frequency generation
$\mathbf{P}$	polarization
$\mathbf{p}$	induced dipole moment
$\mathbf{E}$	electric field
ε_0	permittivity of free space
$\boldsymbol{\chi}^{(2)}$	second order non linear susceptibility
$\boldsymbol{\chi}^{(2)}_{\text{eff}}$	effective second order non linear susceptibility
ω	wavenumber
IR	infrared
vis	visible
$\mathbf{L}$	macroscopic local field factor
FTIR	Fourier-transform infrared
MD	molecular dynamics
NVT	canonical ensemble
NPT	isothermic-isobaric ensemble
PCM	polarizable continuum model
ρ	Raman depolarization ratio
R	hyperpolarizability ratio $\alpha^{(2)}_{aac}/\alpha^{(2)}_{ccc}$
$\boldsymbol{\alpha}$	linear polarizibility
$\boldsymbol{\alpha}^{(2)}$	hyperpolarizibility
θ	tilt angle
ψ	roll angle
ϕ	in-plane rotation
n	refractive index

n'	interfacial refractive index
ε'	interfacial dielectric constant
AIMD	*ab initio* molecular dynamics
DFT	density functional theory
i, j, k	placeholder for lab frame Cartesian coordinates
x, y, z	lab frame Cartesian coordinates
l, m, n	placeholder for molecular frame Cartesian coordinates
a, b, c	molecular frame coordinates
Ω	polarizer angle
PNA	polarization null angle

Acknowledgements

Firstly I would like to thank my supervisor and mentor Dr. Dennis Hore, who has guided me in this first step of becoming an independent researcher. I am incredibly grateful to my family for giving inspiration, and for lending their life experience in graduate studies and academic research; but especially to my father Dr. Stephenson Yang who has guided my scientific journey. Then to my friends (personal and academic), who I could not have completed this degree without. Finally my dog Tika,[1] for being a very silly doggie.

[1] Sometimes spelt Toika in other texts.

Dedication

To my dog Tika.

Chapter 1

Introduction

1.1 Interfaces

Understanding the structure of interfacial systems is crucial as there is a massive divergence in phenomena compared to the bulk environment [1, 2]. Chemically, one can expect to see reactions proceed many orders of magnitude faster under interfacial conditions [3], these unique properties arise from the inherent anisotropy present in such environments. In particular water, one of the most complex liquids, becomes more intricate at the interface [4]; however, with such complexity comes great difficulty in its experimental study. Various methods exist, however most either disturb the interface such as atomic force microscopy, cannot be performed under realistic ambient conditions (for example under vacuum), or simply cannot achieve the specificity needed to study the 1 nm region as is the case with Fourier-transform infrared spectroscopy. Some effective methods are second-order based optical effects, such as second-harmonic generation or vibrational sum frequency generation (SFG); of these two options sum frequency generation is the clear choice due to the additional benefits that probing vibrational modes gives.

1.2 Sum frequency generation

In linear optics the polarization **P** to an induced field can be written as

$$\mathbf{P}(\omega) = \varepsilon_0 \boldsymbol{\chi}^{(1)} \mathbf{E}(\omega). \tag{1.1}$$

Where we refer to $\boldsymbol{\chi}^{(1)}$ as the linear susceptibility, and ε_0 being the permittivity of free space. An example of a $\boldsymbol{\chi}^{(1)}$ effect would be infrared absorption. We will be referring to all $\boldsymbol{\chi}^{(i)}$ with $i = 1$ as linear, and non linear with $i \geq 1$. With a strong enough applied field we can expand the polarization as a power series leading to [5]

$$\mathbf{P}^{(1)}(\omega) + \mathbf{P}^{(2)}(\omega) + \cdots = \varepsilon_0 \left(\boldsymbol{\chi}^{(1)} \mathbf{E}(\omega) + \boldsymbol{\chi}^{(2)} \mathbf{E}(\omega)^2 + \cdots \right). \tag{1.2}$$

We will be focusing in second order responses; which begs the question why would one be interested in a second order response? We illustrate one of the main advantages by taking the negative of $\mathbf{P}^{(2)}$ i.e, by applying the field in the reverse direction

$$-\mathbf{P}^{(2)} = \varepsilon_0 \boldsymbol{\chi}^{(2)} \left(-\mathbf{E}(t)\right)^2. \tag{1.3}$$

Then, if the material is centrosymmetric, $\boldsymbol{\chi}^{(2)}$ must be equal in both directions

$$\implies \mathbf{P}^{(2)}(t) = -\mathbf{P}^{(2)}(t) \implies \mathbf{P}^{(2)}(t) = 0 = \varepsilon_0 \boldsymbol{\chi}^{(2)} \mathbf{E}(t)^2 \implies \boldsymbol{\chi}^{(2)} = 0 \tag{1.4}$$

therefore in any material with some form of centrosymmetry we can expect no overall contribution to the $\boldsymbol{\chi}^2$ tensor [5–7] it is trivial to show this is true for any even order element of $\boldsymbol{\chi}$. This illustrates the main benefit, the inherent interfacial specificity. For example in the case of a liquid-air interface, mathematically there must be some inherent centrosymmetry breaking region, meaning if we assume the bulk region to be isotropic all of the $\boldsymbol{\chi}^{(2)}$ signal must arising from the interfacial region. However, it is possible for there to be some bulk contribution to $\boldsymbol{\chi}^{(2)}$, but that is outside the scope of this text, (see Ref. [7] for more details). Now, if we consider the specific case of vibrational sum-frequency generation, we gain additional insight from vibrational resonance in a similar fashion to traditional infrared or spontaneous Raman measurements. A vibrational SFG experiment generally involves two

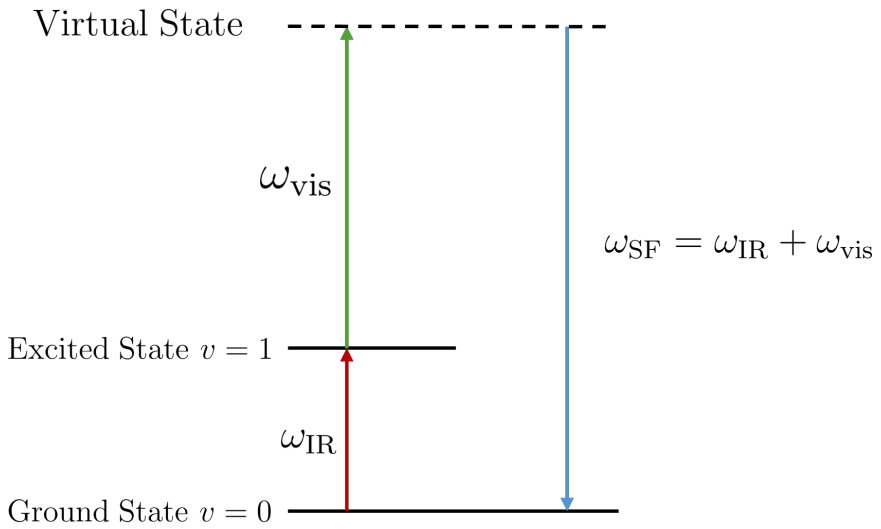

Figure 1.1: Energy level diagram of vibrational SFG off electronic resonance. Two incident photons (one at infrared and one at visible) are combined to release one photon at a frequency that is the sum of the previous two.

lasers of which one is on vibrational resonance and normally one in the visible region off electronic resonance. In Fig. 1.1 we observe the first two photons being destroyed, where then a new photon with a frequency that is the sum of the previous two is emitted. We also know the momentum of the emitted photon given that sum frequency generation is a parametric process (meaning the beginning and end quantum states are the same). We can then describe the second order polarization as

$$P_i^{(2)}\left(\omega_{\text{IR}} + \omega_{\text{vis}} = \omega_{\text{SFG}}\right) \propto \sum_{j,k}^{x,y,z} \chi_{ijk}^{(2)} E_{\text{vis},j} E_{\text{IR},k} \tag{1.5}$$

where i, j, k are any of the Cartesian lab-frame coordinates [6]. On the molecular scale we can write the second order non linear susceptibility as

$$\begin{aligned} \chi_{ijk}^{(2)} &= \frac{1}{\varepsilon_0} \sum_{\text{molecules}} \alpha_{ijk}^{(2)}(\omega_{\text{IR}}, \omega_{\text{vis}}) \\ &= N\langle \alpha_{ijk}^{(2)}(\omega_{\text{IR}}, \omega_{vis})\rangle \end{aligned} \tag{1.6}$$

Where $\boldsymbol{\alpha}^{(2)}$ is the molecular second order susceptibility, normally referred to as the hyperpolarizability more discussion of the hyperpolarizibility is available in Chapter 5). Analogous to the macroscopic case, we can write the induced dipole moment as a power

series expansion [5, 6, 8]

$$\mathbf{p}^{(1)} + \mathbf{p}^{(2)} + \cdots = \boldsymbol{\alpha}^{(1)}\mathbf{E}(t) + \boldsymbol{\alpha}^{(2)}\mathbf{E}(t)^2 + \cdots \tag{1.7}$$

where $\boldsymbol{\alpha}^{(1)}$ is the linear polarizibility. Now if we consider the effective irradiance of the SFG beam, we can then write

$$I(\omega_{\mathrm{IR}} + \omega_{\mathrm{vis}}) \propto \left|\boldsymbol{\chi}^{(2)}_{\mathrm{eff}}\right|^2 I(\omega_{\mathrm{vis}})I(\omega_{\mathrm{IR}}). \tag{1.8}$$

Notice the use of $\boldsymbol{\chi}^{(2)}_{\mathrm{eff}}$ in lieu of $\boldsymbol{\chi}^{(2)}$. This is due to the incident electric field being different from where the SFG is generated. We refer to this corrected susceptibility as the effective second order non linear susceptibility, so called as this is the measured quantity. We can write the correction as

$$\chi^{(2)}_{\mathrm{eff}} = L_{ii}\chi^{(2)}_{ijk}L_{jj}L_{kk} \tag{1.9}$$

where the $\mathbf{L}$ components are known precisely as the macroscopic local field factors.

For the x, y components the definition is simple due to the lack of discontinuity in the xy plane. We have

$$L_{xx} = \frac{E_{z=0}}{E_i}\cos(\theta_i)\cos(\Omega) = (1 - r_{\mathrm{p}})\cos(\theta_i)\cos(\Omega) \tag{1.10}$$

and similarly

$$L_{yy} = \frac{E_{z=0}}{E_i}\sin(\Omega) = (1 + r_{\mathrm{s}})\sin(\Omega). \tag{1.11}$$

where r are the Fresnel coefficients for reflection, θ_i is the angle of incidence (in the case of IR or visible lasers) or reflection in the case of the SFG beam. Now for L_{zz} we must contend with the discontinuity in the interface. First we can define L_{zz} above the interface as

$$L^{0^+}_{zz} = \frac{E_{z=0^+}}{E_i}\sin(\theta_i)\cos(\Omega) = \left(1 + r_{\mathrm{p}}\right)\sin(\theta_i)\cos(\Omega). \tag{1.12}$$

and below

$$L^{0^-}_{zz} = (1 + r_{\mathrm{p}})\frac{n_1^2}{n_2^2}\sin(\theta_i)\cos(\Omega). \tag{1.13}$$

Therefore at the interface it is convention to define an interfacial refractive index n' and therefore [6, 7, 9]

$$L_{zz} = (1 + r_{\mathrm{p}})\frac{n_1^2}{n'^2}\sin(\theta_i)\cos(\Omega). \tag{1.14}$$

There will more discussion of this parameter later. If we now turn our attention back to the $\boldsymbol{\chi}^{(2)}$ tensor, we can see that there are 27 independent elements. However if we make the assumption of C_{3v} symmetry of the vibrational mode we can reduce the problem to only 3 independent elements (the derivation of this is in Chapter 5). [9, 10]: $\chi^{(2)}_{yyz}$, $\chi^{(2)}_{yzy}$, and $\chi^{(2)}_{zzz}$. Then if we take note that beams in the P polarization can probe E_z and E_x, while S probes E_y, we can write the expressions for the most common polarization combinations, taking note that by convention the first letter in the subscript corresponds to the polarization plane of the SFG polarizer, visible the second, and finally IR.

$$\chi^{(2)}_{\mathrm{eff,SSP}} = \sin(\Omega)\sin(\Omega_{\mathrm{vis}})\cos(\Omega_{\mathrm{IR}})L_{yy}L_{yy}L_{zz}\chi^{(2)}_{yyz} \tag{1.15}$$

$$\chi^{(2)}_{\mathrm{eff,SPS}} = \sin(\Omega)\cos(\Omega_{\mathrm{vis}})\sin(\Omega_{\mathrm{IR}})L_{yy}L_{zz}L_{yy}\chi^{(2)}_{yzy} \tag{1.16}$$

$$\begin{aligned}\chi^{(2)}_{\mathrm{eff,PPP}} = \cos(\Omega)\cos(\Omega_{\mathrm{vis}})\cos(\Omega_{\mathrm{IR}})(&-L_{xx}L_{xx}L_{zz}\chi^{(2)}_{yyz} - L_{xx}L_{zz}L_{yy}\chi^{(2)}_{yzy} \\ &+ L_{zz}L_{xx}L_{xx}\chi^{(2)}_{yzy} + L_{zz}L_{zz}L_{zz}\chi^{(2)}_{zzz})\end{aligned} \tag{1.17}$$

Ω is defined as the polarizer angle; here we have $\Omega = 90^\circ$ as S and $\Omega = 0^\circ$ as P. We define S to be perpendicular to the plane of incidence (from senkrecht in German) while P is parallel. Now by using the above and Eq. 1.8, we arrive at the common formulation for the SFG intensity [6, 7, 9, 10]

$$I(\omega_{\mathrm{IR}} + \omega_{\mathrm{vis}})_{SSP} \propto \left|L_{yy}L_{yy}L_{zz}\chi^{(2)}_{yyz}\right|^2 I(\omega_{\mathrm{vis}})I(\omega_{\mathrm{IR}}). \tag{1.18}$$

1.3 Molecular dynamics

In brief, the idea behind molecular dynamics comes from the fact that many problems in statistical mechanics are not explicitly solvable [11], especially as the complexity increases.

For example, liquid water compared to an Einstein crystal where for the latter we can calculate all the thermodynamic properties explicitly. Therefore in order to study such systems, we look towards computer assistance to simulate their properties. Different computational tools exist. In molecular dynamics we are solving Newton's equations of motion with the assistance of a potential to calculate the net acceleration of the atoms. Furthermore the system is placed under some form of thermodynamic ensemble, for example canonical (also known as NVT), or isothermal-isobaric (known as NPT). The velocity is corrected for by the thermostat, which effectively regulates the temperature of the system. The pressure can be regulated by a barostat which in effect changes the size of the simulation box to ensure the pressure is constant. Of course the method in which these algorithms are applied is much more complicated, although they mostly operate in a similar fashion to as described here. The way the forcefield or potential is calculated varies; in fact, we separate them into two categories: classical where interactions between atoms behave as balls on springs which is referred to as molecular mechanics (colloquially, when one refers to molecular dynamics it is almost always classical), and *ab initio* where the potential is calculated using quantum calculations. Generally the first step in any MD workflow starts with an energy minimization. To avoid any strange conflict (such as overlap) between atoms, normally one uses steepest descent or conjugate gradient to do this. Then an equilibration is run where we let the thermodynamic properties settle, for example at 300 K and 1 bar, the equilibration is generally run with the same parameters as the production run, however just until the parameters converge. Because we only have computing power to simulate a limited number of atoms, we apply periodic boundary conditions, roughly analogous to the game of pac-man which allows for the approximation of an infinite system. In the proceeding chapters we will be considering interfacial systems; in that case we are changing the size of the box in the $\hat{z}$ direction which will create two liquid-vacuum interfaces, although applying a barostat in that case is impossible.

1.3.1 Classical molecular dynamics

Historically, classical simulations have their roots in molecular mechanics where atoms (generally they are more separate than atoms, for example an sp^2 carbon is not treated in the same way as an sp^3) are treated as balls and springs. Importantly, molecular mechanics does not refer to any sort of dynamical behavior and is much more akin to a energy minimization. But from molecular mechanics we can define classical molecular dynamics by the use of forcefield potentials with the addition of a thermodynamical ensemble. The forcefields define the intermolecular forces (such as covalent bonds) but also intramolecular forces (such as Van der Waals). These forcefields are commonly calibrated with some form of quantum calculation, but can also be parameterized with tools such as machine learning [12]. These forcefields come in many different flavours depending on application. For example they may not treat every atom individually but instead as one unit of atoms. The choice of forcefield is system and computing resource dependant, and has a drastic effect on the evolution and trajectory of the system [11]. In general most forcefield-based approaches are ill-equipped to solve any problem where we would expect some form of quantum interaction (such as bond formation and breaking, or any new interaction where the forcefield has not been parameterized for. [13].

1.3.2 *Ab initio* molecular dynamics

The main difference between classical and *ab initio* at least in the case of the Born-Oppenheimer approximation (this means the energies are additive). Is simply the forcefields or potential, otherwise there is not much difference between them. One can think of *ab initio* MD as simply calculating the forcefields on the fly at each time step using (in general) density functional theory methods. Then the usual considerations of basis set and functional choice apply; with the added caveat given the amount of times the potentials must be calculated, a lower level of theory is necessary. Another difference would be in system size, for example in this text our *ab-inito* system has a volume of 8 nm^3, while

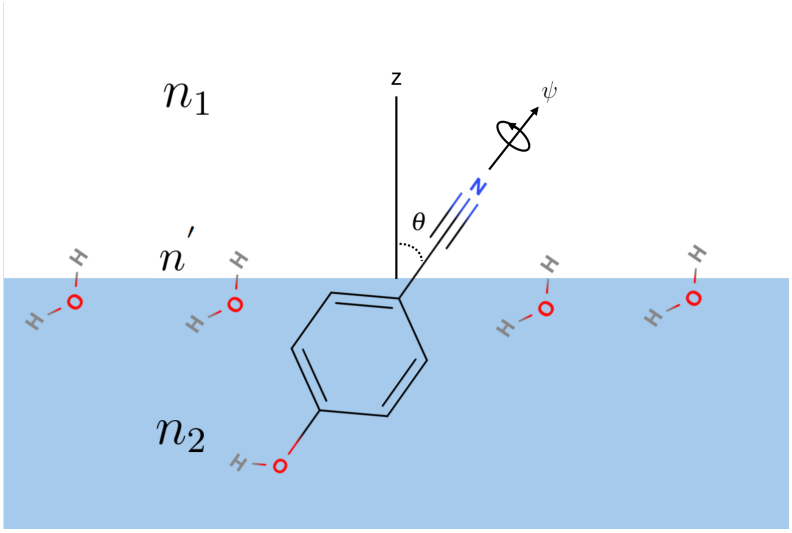

Figure 1.2: Diagram of p-cyanophenol at the air-water interface. The tilt angle θ and roll angle ψ are defined. The approximate locations of the three refractive indices (n_1, n_2, n') are also given.

entire viruses have been studied [14] using classical molecular dynamics.

1.4 Outline of thesis

The behavior and electronic structure of p-cyanophenol at the vapor solution interface (as in Fig. 1.2) is the focus of our inquiry, where orientational (θ, ψ), linear optical (n') and electronic ($R = \alpha^{(2)}_{aac}/\alpha^{(2)}_{ccc}$) properties are elucidated. In Chapter 3 the orientation distribution and the effect of changing surface number density is studied. Chapter 4 is focused on the depth dependence of the interfacial refractive index. The hyperpolarizibility ratio is studied using density functional theory and SFG measurements in Chapter 5, and with *ab initio* molecular dynamics in Chapter 6.

Chapter 2

Methods

2.1 Classical molecular dynamics and refractive index

The goal is to simulate the orientation distribution and volume fraction distribution of cyanophenol at the vapor solution. This can be done by simulating a bulk solution, and then extending the simulation box to create two interfacial regions as in Fig. 2.1. Classical MD simulations were performed using GROMACS [15] with the OPLS-AA forcefield for para-cyanophenol, [16] and the TIP4P water model [17]. The cyanophenol topology was generated using the LigParGen software [18–20]. A box with dimensions of 9 nm $\times$ 9 nm $\times$ 9 nm was created and filled with 216 cyanophenol molecules. The box was then solvated with 22,850 TIP4P water molecules. This produced a cyanophenol surface number density that was selected based on literature surface tension data [21]. Following a minimization, an NVT equilibration and then NPT equilibration run was carried out. The box was then extended to a dimension of 15.3 nm in the z direction in order to create two vapor–solution interfaces as in Fig. 2.1. This was then followed by an additional minimization and NVT equilibration. Equilibrium trajectories using a 2 fs integration step size were acquired for 1 ns using a Nose-Hoover thermostat [22] and Parrinello-Rahman barostat [23]. The NVT production run was 20 ns in duration, with a step size of 2 fs. A snapshot was taken every 0.04 ns leading to 501 data frames available for analysis. For the volume fraction determination, the molar volume of water was taken to be 18.07 $cm^3 \cdot mol^{-1}$. The molar volume of cyanophenol was calculated using the B3LYP functional [24, 25] with a aug-cc-

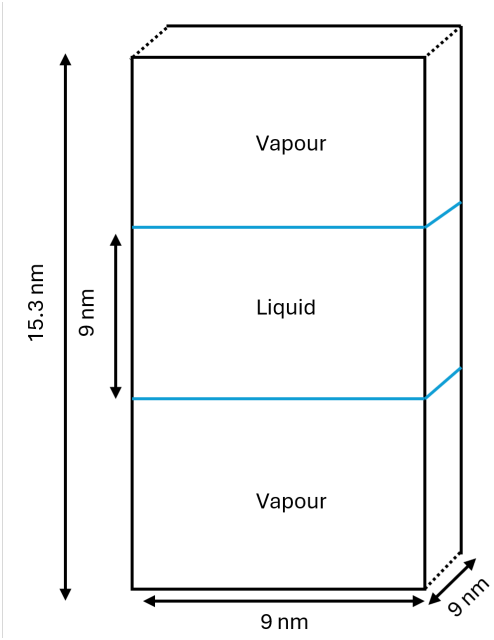

Figure 2.1: Schematic of system for classical molecular dynamics. Blue lines describe the system before extension in the z-axis. The three dimensional periodic boundary conditions are applied at the lines.

PVTZ basis set [26] using Gaussian 16 [27] giving a value of 98.6 $cm^3 \cdot mol^{-1}$. Variable-width bins were defined such that the number of cyanophenol molecules N in each bin was equal in order to facilitate summation without the need for scaling, to ensure that each bin has sufficient statistics. The orientational parameters $\langle \cos\theta \rangle$ and $\langle \cos^3\theta \rangle$ for each bin i were computed using

$$\langle \cos\theta \rangle_i = \frac{1}{N_i} \sum_{l=1}^{N_i} \cos\theta_i \tag{2.1}$$

$$\langle \cos\theta \rangle_i = \frac{1}{N_i} \sum_{l=1}^{N_i} \cos^3\theta_i \tag{2.2}$$

where the angle θ is taken to be the angle between the surface normal and the cyano bond. The interfacial refractive index was calculated using Eq. 4.7, where the volumes for each bin are taken from above. The reference values for the cyanophenol contribution is taken from an FTIR measurement in Ref. 28 as in Fig. 2.2; in a similar vein, the values for water were taken to be $1.3311 + 0.014i$, and 1.3337 at infrared and visible/SFG frequencies [29].

2.2 Depth dependant binning

Using the depth dependant refractive index (from Eq. 4.7) and the orientational parameters the $\boldsymbol{\chi}^{(2)}_{\text{eff}}$ response was then computed as

$$\chi^{(2)}_{lmn,\text{eff}} = \left| \sum_{p=1}^{n} \left[\left(\text{NR} + \int_0^{\infty} \frac{A_{ijk,p}}{\omega_L - \omega_{\text{IR}} - i\Gamma_{\text{L}}} \exp\left[-\frac{(\omega_{\text{L}} - \omega_0)^2}{2\Gamma_{\text{G}}^2} \right] \mathrm{d}\omega_{\text{L}} \right) LLL_{lmn,p} \right] \right|. \quad (2.3)$$

The homogeneous broadening Γ_{L} is taken to be 2.1 cm^{-1}, the inhomogeneous broadening taken to be 5 cm^{-1} similar to the values chosen in 28. The non-resonant response NR was used as a fitting parameter. One should note that this implies that the non-resonant response is linearly proportional to the number density N of cyanophenol molecules. Given that dispersion in the infrared region of the interfacial refractive index is small (considering the relative volume fractions) and that we are assuming no dispersion in the infrared region of n_2, the approximation is likely adequate for the purposes of fitting the experimental data. The amplitudes are calculated using Eq. 4.8.

2.3 Ab initio molecular dynamics

Two systems of interest were studied using AIMD, with cyanophenol at the interface and in bulk solution. The two cyanophenol systems contained 1 p-cyanophenol molecule and 217 water molecules as a solvent. The systems were equilbrated using classical MD in a similar way to as above, however the starting box size for the cyanophenol systems was 2 nm^3. The cyanophenol systems used the SPC solvation model. The bulk solution phase was considered finished after the NPT equilibration, however the interfacial cyanophenol was expanded to 9 nm in the z direction following NPT equilibration. The interfacial system was then minimized and equilibrated NVT as described in the previous section. After the systems were suitably classically equilibrated, a further two AIMD equilibrations were performed for 1 ps and 15 ps respectively. The first equilibration used a massive thermostat

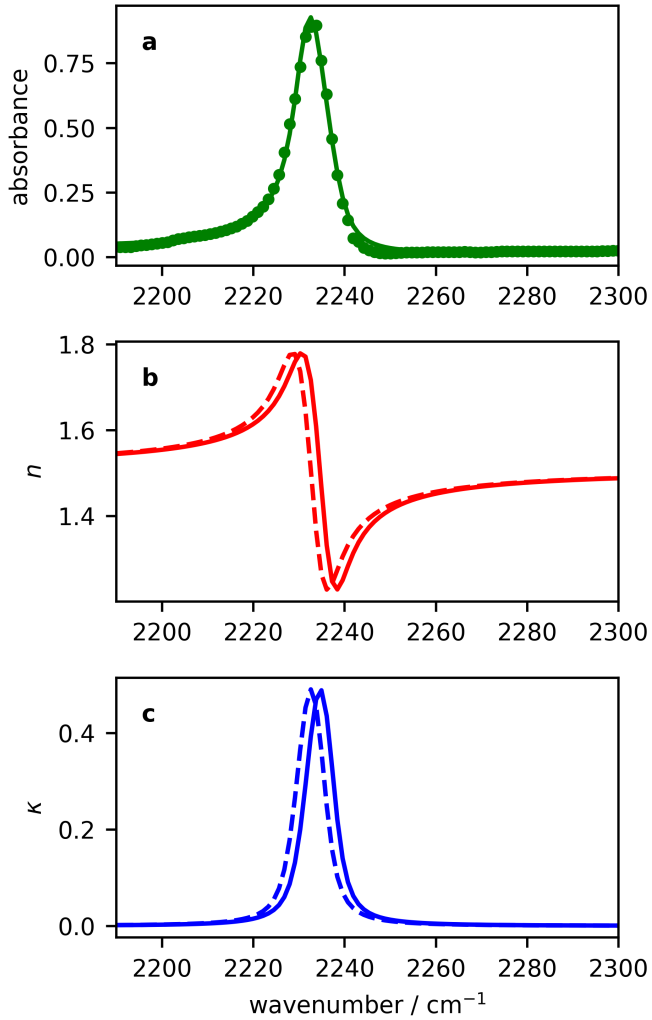

Figure 2.2: (a) Experimental absorbance data in points, (b) real and (c) imaginary components of the para-cyanophenol refractive index plotted with solid lines. Optical constants plotted with dashed lines are derived from the similarly however the resonance frequency is red-shifted by 3 cm^{-1}. Reprinted with permission from Ref. 28. Copyright 2023 American Chemical Society.

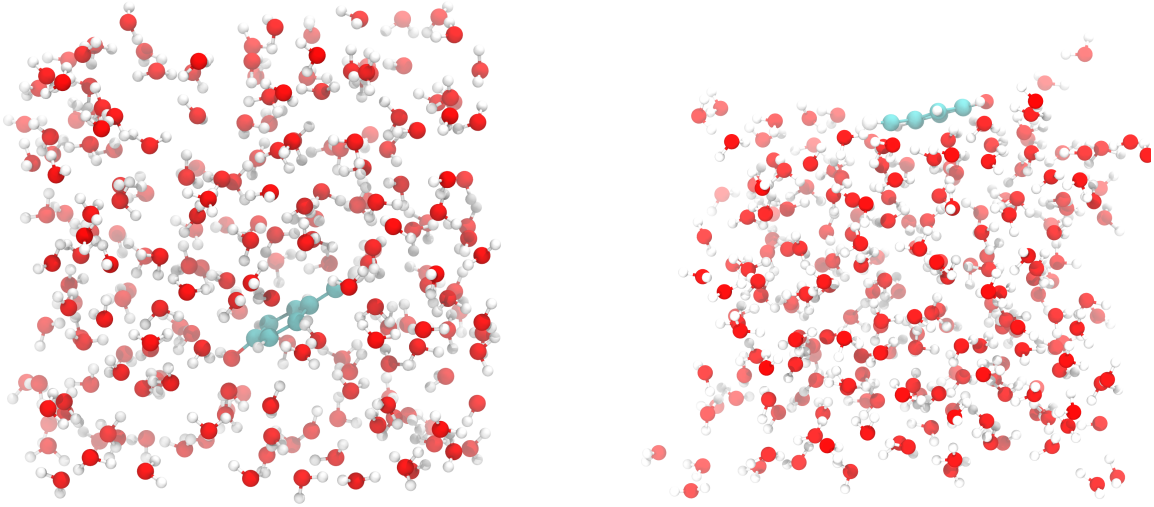

(a) Bulk (b) Surface

Figure 2.3: (a) Snapshot of an *ab initio* molecular dynamics trajectory with cyanophenol in bulk solution with periodic boundary conditions in x, y, z. (b) Snapshot of an *ab initio* molecular dynamics trajectory with cyanophenol at the water-vapor interface with periodic boundary conditions in effectively x, y.

while the second used a global thermostat. The production run proceeded with the same conditions as the second equilibration; however the simulation ran for 80 ps for the surface, and 60 ps for the bulk. All AIMD simulations ran using CP2K QUICKSTEP [30, 31], a, 0.5 fs step size and used GTH-BLYP, and the DZVP-MOLOPT-SR-GTH as the functional and basis-set. After the production run completed, the electron density was calculated every 4 fs which is sufficient for the collection of non-chiral spectra, although shortening the probing step size could provide greater accuracy in modes higher than 2000 cm^{-1} [32]. The electronic properties and Raman spectra could then be calculated using Vornonoi integration [33] as implemented in TRAVIS [34, 35]. The spectra were considered to be converged after 60 ps as the depolarization ratio and spectral shape did not meaningfully change after an additional 20 ps. The differences between the interfacial and bulk systems are illustrated in Fig. 2.3.

2.4 Experimental measurements

The experimental measurements were performed by Aruna Kumarasiri and is outside the scope of this thesis, however the full experimental details are available in the Supporting Information of Ref. 28.

2.5 Density functional theory calculations

For the density functional theory (DFT) calculations of the hyperpolarizibility in Chapter 5, Gaussian 16 was used [27]. In all DFT calculations an optimization, followed by a frequency calculation on the optimized geometry was done to calculate the polarizability derivatives of cyanophenol, benzonitrile, and acetonitrile. All simulations used the B3LYP functional with the aug-cc-TZVP basis set. For the solvated systems, a polarizable continuum model (PCM) solvation for water/organic solvents was applied.

Chapter 3

Orientational Properties of p-cyanophenol

3.1 Introduction

If we consider the main applications of quantitative SFG measurement, the orientational parameters are an obvious choice; such measurements have been done numerous times [9, 10, 36–38]. Whether such measurements are practical to take in the face of such problems as the $\langle P_3 \rangle$ magic angle [39] (analogous to the $\langle P_2 \rangle$ magic in IR and nuclear magnetic resonance which makes all wide distributions appear centered at 39.2°), is outside the scope of this discussion; nevertheless understanding the importance of the orientational contribution to $\boldsymbol{\chi}^{(2)}$ is critical. Firstly we define the Euler angles using the standard definitions found in SFG spectroscopy [40], with θ defined by the angle between the molecular axis (in the case of cyanophenol the C–N bond) and $\hat{z}$ (the surface normal), ϕ as the roll, and ψ as in plane rotation. Looking back at Eq. 1.6 we have an implicit orientational dependence from the expectation value of the hyperpolarizibility. We can then rewrite Eq. 1.6 as

$$\chi^{(2)}_{ijk} = \frac{N}{c\varepsilon_0} \int_0^{2\pi} \int_0^{2\pi} \int_0^{2\pi} f(\theta,\phi,\psi)\, \alpha^{(2)}_{ijk} \sin(\theta)\, \mathrm{d}\theta\, \mathrm{d}\phi\, \mathrm{d}\psi \tag{3.1}$$

one might notice the inclusion of the $\sin\theta$ term, this corresponds to the fact that an isotropic distribution of θ is not uniform, it is instead in the form of a $\sin\theta$ curve. $f(\theta,\phi,\psi)$ is defined as the orientation distribution. Most commonly the orientation distribution is

assumed to be uniform in ϕ and ψ. In such a situation we remove the ψ and ϕ dependence and reduce the issue to an θ only problem. Of course assuming a uniform distribution in ϕ in anything but the most simple linear molecules is questionable; however it reduces the difficulty of the problem significantly. One must take note that the assumption of a θ only problem makes solving for the whole orientation distribution impossible (this is discussed more in Chapter. 5). In such a situation, it is common in SFG literature to refer to the orientation distribution in terms of the expectation values $\langle\cos\theta\rangle$, and $\langle\cos^3\theta\rangle$, which is analogous to infrared with $\langle\cos^2\theta\rangle$ being the main parameter of interest. However in general the systems measured by SFG are non-isotropic, in which case the orientational parameters have a non-trivial effect on the overall signal, of which can be very challenging to disentangle. Instead of trying to quantitatively describe the orientation distribution experimentally, a common method is to compare with classical molecular dynamics simulations; while classical simulations are a large approximation, they still provide a good estimate of the true orientation.

3.2 Orientational analysis

Firstly let us consider the orientation distribution by analysing the complete trajectory with Fig. 3.1. We set this simulation to have roughly a monolayer of cyanophenol based on surface tension measurements [21]; and should roughly match the number density of the experimental data. We do this by taking note of the expected surface number density from surface tension measurements, and then populate our system with twice the amount of cyanophenol molecules which accounts for the two interfacial regions. Importantly, the concentration difference is quite large in comparison to the experimental 75 mmol/L, due to the square cube law, however this should be of no consequence in our measurement as we are only considering the top $\approx$ 1 nm region. We observe the mean angle to be around 70° from the surface normal, indicating a weak orientational preference with respect to the interface. This is likely due to the hydrogen bonding capability of both the O–H and C–N

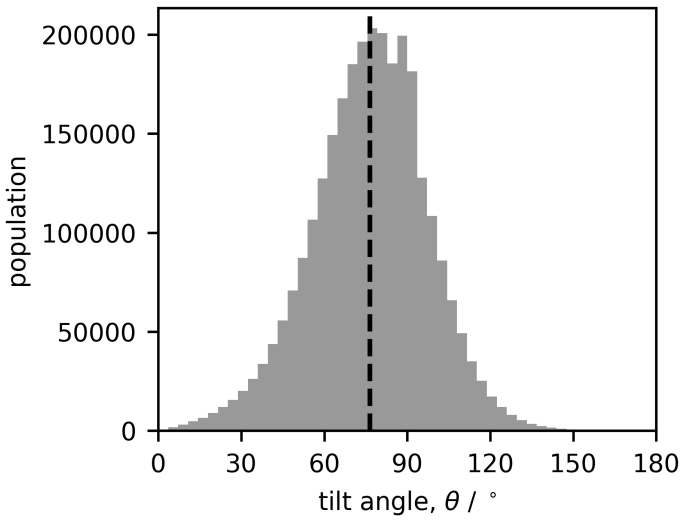

Figure 3.1: Tilt angle distribution constructed from the analysis of 2.8 million C–N bonds from a 20 ns simulation of 216 cyanophenol molecules at the air–solution interface. Reprinted with permission from Ref. 28. Copyright 2023 American Chemical Society.

groups, where the O–H can be considered more favorable. Interestingly if instead of p-cyanophenol where the O–H and C–N groups are opposite with respect to the phenyl ring, we used either ortho or even meta configuration we could likely expect stronger orientation of the C–N group (albeit in the other direction); this could imply a stronger SFG signal. We can also calculate the orientational parameters $\langle \cos\theta \rangle = 0.217$ and $\langle \cos^3\theta \rangle = 0.0767$.

Now we examine the affect of changing surface number density N on the orientation distribution, where one could expect to see a stronger orientational preference as N increases. However from Fig. 3.2 we fail to see major changes even when increasing the density by a factor of 100. Furthermore any difference could be easily rationalized by the difference in statistics in the four simulations. Now we can confidently conclude that the solvation of water is the strongest factor with respect to ordering the cyanophenol molecules. In the largest simulation with $N = 500$ it is likely that many cyanophenol molecules are forced into the bulk environment instead of contributing to the ordering. Previous SFG measurements see little difference in signal after 75 mmol/L, which corresponds to a surface number density of 216. Of course there should be significant

differences in the dielectric profile in a full monolayer compared to incomplete coverage, but if accounted for we should expect a linear relationship between the concentration of cyanophenol and the experimental SFG response. This also gives credence to our one cyanophenol *ab initio* molecular dynamics system being representative of a full monolayer in Chapter 5.

Finally with respect to the roll angle, even though for a $C_{\infty v}$ system the roll has no effect on the overall intensity, it is still of intellectual interest. Importantly, by convention we define $\psi = 0^\circ$ to be where the phenyl ring is parallel with respect to the interface; from symmetry of the mirror plane in the cyanophenol molecule -180° and -180° are also equivalent to 0°. From Fig. 3.3 we observe a preference for the phenyl ring to lay flat along the interface. This is likely similar to the preference of a benzene ring to also be flat at the interface as measured by Ref. 41 in a computational study. We can rationalize this by assuming the hydrophobic nature of the phenyl ring prefers to reduce the overlap with water as much as is possible. We can assume that only the highest cyanophenol molecules have such a preference, as if the cyanophenol becomes more solvated (but still surface active) such a preference is unlikely.

3.3 Conclusion

By analysing classical molecular dynamics trajectories we were able to ascertain orientational properties of cyanophenol at the water-vapor interface. For a full monolayer, cyanophenol is relatively flat with an average tilt angle of 76.4° likely due to the hydrogen bonding of both the O–H and C–N groups. The orientation distribution did not vary much with increasing surface number density, indicating that water dominates the ordering of cyanophenol. The population density of the roll angle was maximized where the cyanophenol was parallel to the interface due to the hydrophobicity of the phenyl ring.

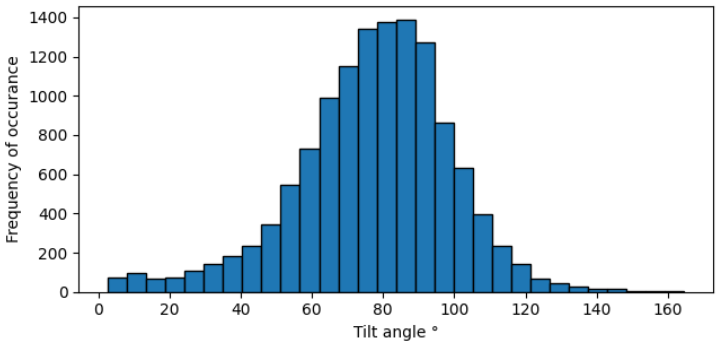

$N = 5$

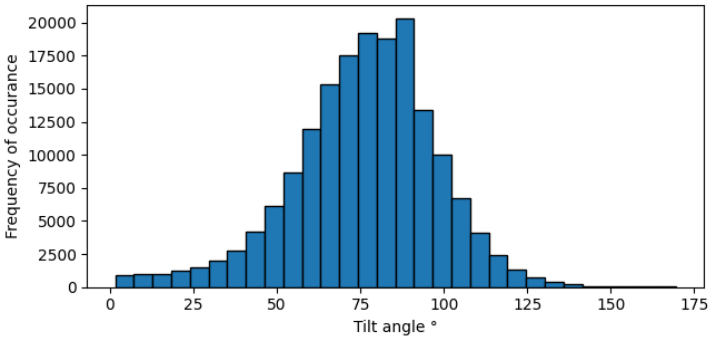

$N = 50$

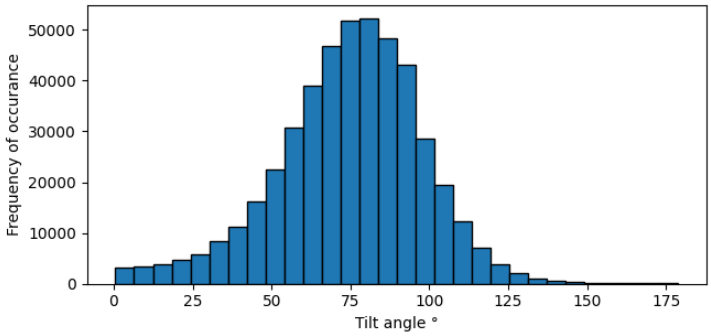

$N = 150$

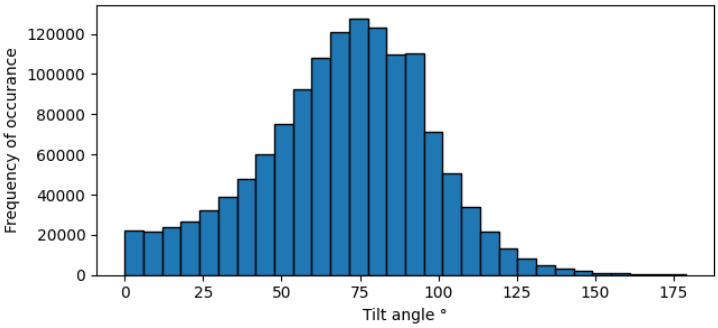

$N = 500$

Figure 3.2: Tilt angle θ histograms with varying number density N cyanophenol molecules. All histograms have been corrected for the $\sin\theta$ isotropic distribution.

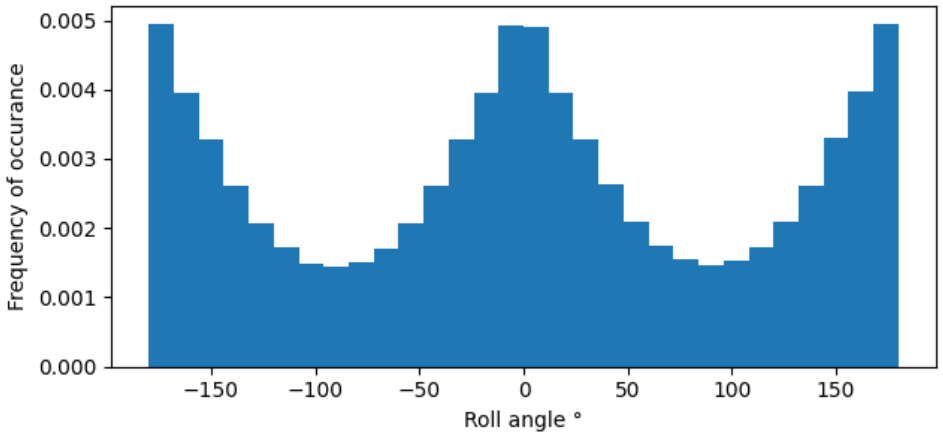

Figure 3.3: Surface roll distribution of 216 p-cyanophenol molecules with surface density of ≈ 76 Å^2.

Chapter 4

Depth-Dependence of the Second Order Effective Nonlinear Susceptibility[1]

4.1 Introduction

With the emergence of surface specific second harmonic measurements in the late 1970s, the characterization of the linear optical properties essential for quantitative analysis has been a challenge. Specifically a parameter known as the interfacial refractive index n' (or dielectric constant), which phenomenologically describes the interface. However whether the surface can be described by such a macroscopic property as the refractive index is questionable, instead a microscopic description can be given

$$\sqrt{n'} = \varepsilon' = \frac{f_x}{f_z} = \frac{f_y}{f_z} \tag{4.1}$$

where f_z and f_y are the microscopic local field factors. The definition of such local field factors is complex; however, a complete description and derivation is available in Ref. 6. One can think of the microscopic local field factors as a correction to $L_{ii}E_i$ that takes the microscopic variation into account (in the macroscopic theory this correction is n'). Deriving relationships of such microscopic field factors is challenging although has been done [42]; a common formulation would be the direct calculation using the Lorentz

[1] Reproduced in part from Yang, P.; Kumarasiri, A.; Hore, D.K. "Surface Populations as a Model for the Distance-Dependence of the Interfacial Refractive Index" *J. Chem. Phys.*, **161**, 054703 (2024) Copyright 2024 AIP Publishing.

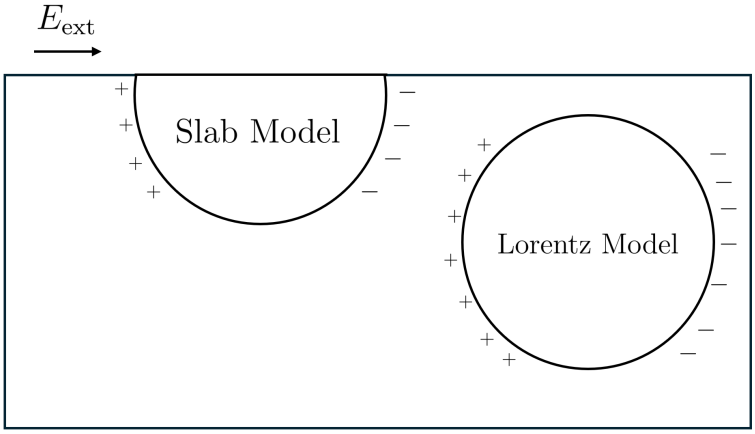

Figure 4.1: Diagram of slab and Lorentz models. The chromophore is represented by either a circle or semicircle.

model [6, 36] leading to

$$n' = \frac{4n_2^2+2}{n_2^2\left(n_2^2+5\right)}. \tag{4.2}$$

Sometimes this model is also known as the slab model owning to the fact that chromophore is assumed to be in a hemisphere where half is solvated; confusingly the model where the chromophore is completely solvated is known as the Lorentz model which is simply

$$n' = n_2 \tag{4.3}$$

Diagrams of both the Lorentz and slab models are avaliable in Fig. 4.1. The Lorentz model is commonly used in polymer or solid interfaces, however given that we are assuming the entire $\boldsymbol{\chi}^{(2)}$ response is arising from some form of anisotropy in the interfacial region, it is likely incorrect to use a bulk property. To combat this problem, other macroscopic descriptions of n' have emerged. One of the most common is simply to take the arithmetic average between the two bulk phases

$$n' = \frac{n_1+n_2}{2} \tag{4.4}$$

which for some problems (such as the orientation distribution) have given somewhat reasonable (by reasonable we mean can be rationalized by chemical intuition) quantitative measurements [43]. Of course such an approximation does not have much actual basis in

the physical reality of the system and is instead a way of avoiding the difficult problem of describing the actual interfacial environment. Thus far all the models implicitly assume some form of binary system (for example water–vapor), however there are many systems (such as the presence of a monolayer at the water–vapor interface) where such a description would not apply. This is exasperated in the infrared region where the dispersion of the resonant species would not be accounted for.

Previously we calculated the overall SFG response using the Lorentz-Lorenz mixing model for the interfacial refractive index (Eq. 4.7), however since the approach was only experimental, the actual volume fractions were an unknown parameter and were all evaluated. Furthermore at first since no experimental data on the orientational parameters was known, all of the amplitudes were considered to be fitting parameters. This effectively allowed for the correspondence between the volume fractions, the interfacial refractive index, and n' as shown in Fig. 4.2. Unfortunately, given the high amount of freedom given to the optimizer every situation with the same amount of dispersion in n' will result in the same fit to the experimental data. This is due to the fact that the amplitudes are not constrained and that the only other source of dispersion is the cyanophenol contribution to n'. This does not only allow for limited insight into the structure of the interface, but also gives a large range of possibilities for the hyperpolarizibility ratio R (more discussion of the hyperpolarizibility ratio in Chapter 5). At first the solution was to constrain the amplitudes using orientational parameters $\langle \cos\theta \rangle$ $\langle \cos^3\theta \rangle$ collected from classical MD simulations which does significantly lower the range of possibilities of n', as shown by the MD simulation range in Fig. 4.2. Importantly however, when the actual volume fractions are taken from the same MD simulation, the situation is different; the spectra no longer has a good fit to the PPP data evidenced by the 1 bin fit in Fig. 4.5. Therefore a new approach was needed, the solution being the separation of the SFG response according to the depth. In particular the interfacial refractive index must be thought of as depth-dependant.

In recent years work has been done in order to fully describe the dielectric profile of

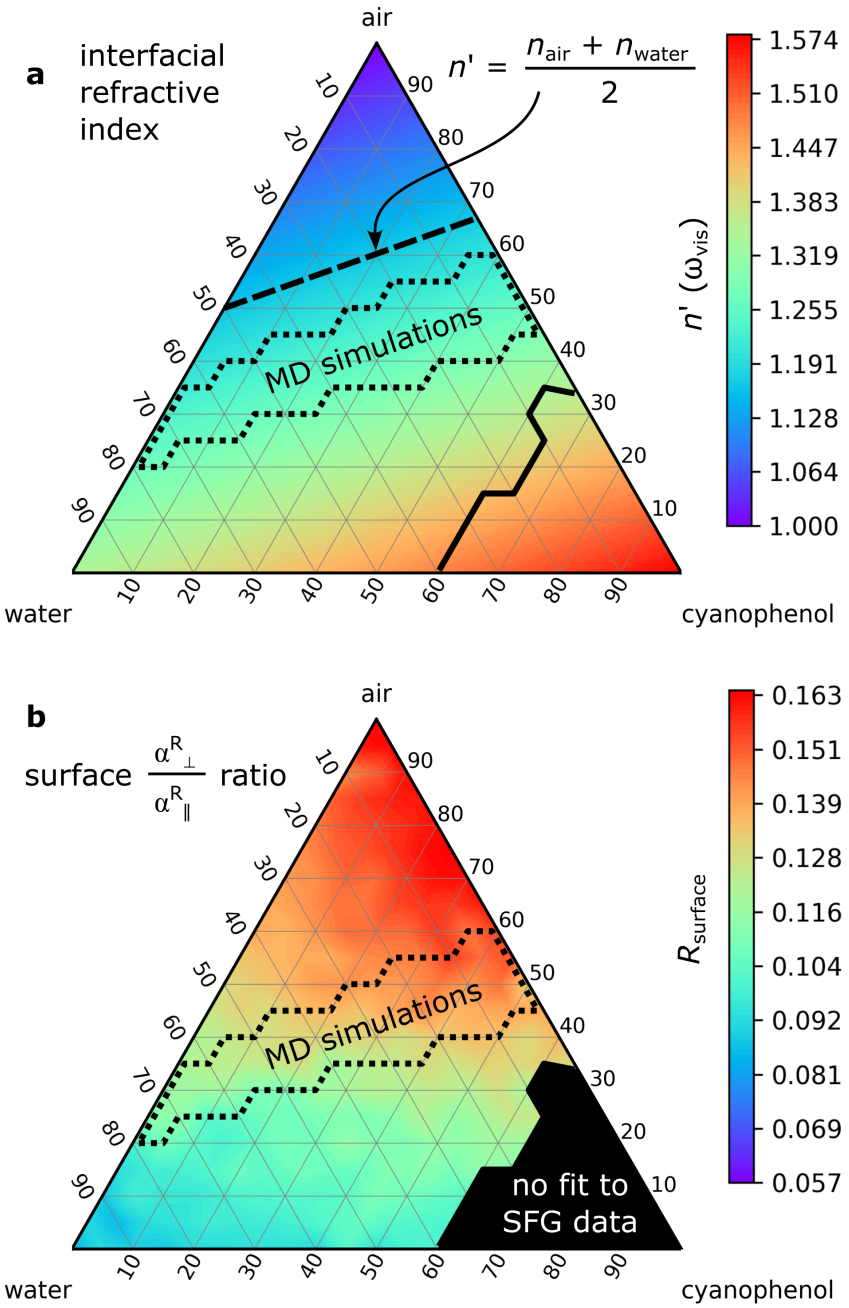

Figure 4.2: (a) Ternary plot of the interfacial refractive index as function of the volume fractions of air, water, and cyanophenol using the Lorentz-Lorenz mixing model. (b) Hyperpolarizability ratio as a function of amplitudes fit using the corresponding interfacial refractive index calculated from the volume fractions. Reprinted with permission from Ref. 28. Copyright 2023 American Chemical Society.

especially aqueous interfaces. Interestingly, the majority of such progress has focused upon the static dielectric profile, which has been studied with a wide range of techniques, from atomic force microscopy to molecular dynamics [44, 45]. However since SFG is generated at IR / visible wavelengths such static descriptions are not directly useful in our analysis; although static profiles do inform about the polarization and thus structure of water. Previously Morita has used molecular dynamics and particle mesh ewald summation to explicitly calculate the microscopic local field factors as a function of depth [6,46], which by Eq. 4.1 gives the depth profile of the refractive index. Importantly, while Morita did calculate $\mathbf{P}^{(2)}$, the actual SFG response was not calculated, and this approach still requires literature values of the hyperpolarizibility. In the future perhaps AIMD calculations which provide the lineshape and hyperpolarizibility could then be combined with such a microscopic description to explicitly calculate the entire $\boldsymbol{\chi}^{(2)}_{\text{eff}}$ response. Nagata *et al* have also developed a few methods to probe the depth dependence of n'. The first approach is to split the SFG response for the water–vapor interface into the various hydrogen bonded species, for example DDAA where the D and A refer to donor or acceptor hydrogen bonding modalities. This is effectively a depth profiling as H_2O molecules close to the interface will in general have less hydrogen bonds [47,48]. The second approach is a model for the depth dependant interfacial refractive index largely similar to the Lorentz and slab models. Unfortunately the depth could not be disentangled from the $\boldsymbol{\chi}^{(2)}$ response, and as a result they could only probe the average depth of the chromophore [49, 50].

4.2 Interfacial refractive index

Fig. 4.3a illustrates the volume fractions of cyanophenol f_{CP}, water f_{W} and air $1 - f_{\text{CP}} - f_{\text{W}}$ as a function of distance across the interface, determined from MD data plotted in points. Here the bulk aqueous phase exists at $z = -\infty$ and $z = 0$ is the Gibbs dividing surface that

was located by fitting the water data to the empirical relationship

$$f_{\mathrm{W}} = A_{\mathrm{W}}\left[1 - \frac{1}{1+\mathrm{e}^{-k_{\mathrm{W}}(z-z_0)}}\right] + b_{\mathrm{W}} \tag{4.5}$$

and solving for z_0; this is plotted with the blue solid line. A_{W}, k_{W} and b_{W} are parameters associated with the amplitude, steepness, and offset that are determined in the fitting but are not of direct interest apart from their necessity in obtaining z_0.

The data in Fig. 4.3a clearly shows that all of the cyanophenol SFG response is generated over a distance of approximately 1 nm, significantly smaller than the nonlinear coherence length. This means that no wavevector mismatch needs to be considered in adding values of the susceptibility $\boldsymbol{\chi}^{(2)}(z)$ obtained at different depths throughout the interface, and the entire system can be described by an effective susceptibility given by $\chi^{(2)}_{ijk,\mathrm{eff}} = L_{ii}L_{jj}L_{kk}\chi^{(2)}_{ijk}$, as long as the $\mathbf{L}$ factors do not display any z-dependence. This is reasonable for

$$L_{xx} = \pm(1-r_{\mathrm{p}})\cos\theta \tag{4.6a}$$

$$L_{yy} = 1 + r_{\mathrm{s}} \tag{4.6b}$$

$$L_{zz} = (1+r_{\mathrm{p}})\left(\frac{n_1}{n'}\right)^2 \sin\theta. \tag{4.6c}$$

where r_{p} and r_{s} are the p- and s-polarized Fresnel reflection coefficients, [51] as they are based on the bulk air (n_1) and water (n_2) refractive indices. However one must consider the influence of n' on L_{zz}. This originates from the fact that, while the tangential components of the electric fields are continuous across the surface, there is no such requirement for E_z that can exhibit a sharp discontinuity at $z = 0$. This creates a complication, as it is precisely in the neighborhood of $z = 0$ that the SFG field is generated. We evaluate n' using a Lorenz-Lorentz mixing model based on the MD simulation volume fractions

$$\frac{n'^2-1}{n'^2+2} \approx f_{\mathrm{W}}\left(\frac{n_{\mathrm{W}}^2-1}{n_{\mathrm{W}}^2+2}\right) + f_{\mathrm{CP}}\left(\frac{n_{\mathrm{CP}}^2-1}{n_{\mathrm{CP}}^2+2}\right). \tag{4.7}$$

One benefit of using Eq. 4.7 is that it provides a facile route for incorporating frequency-dependent refractive index data to model the dispersion of n'. [52–55] This enables us

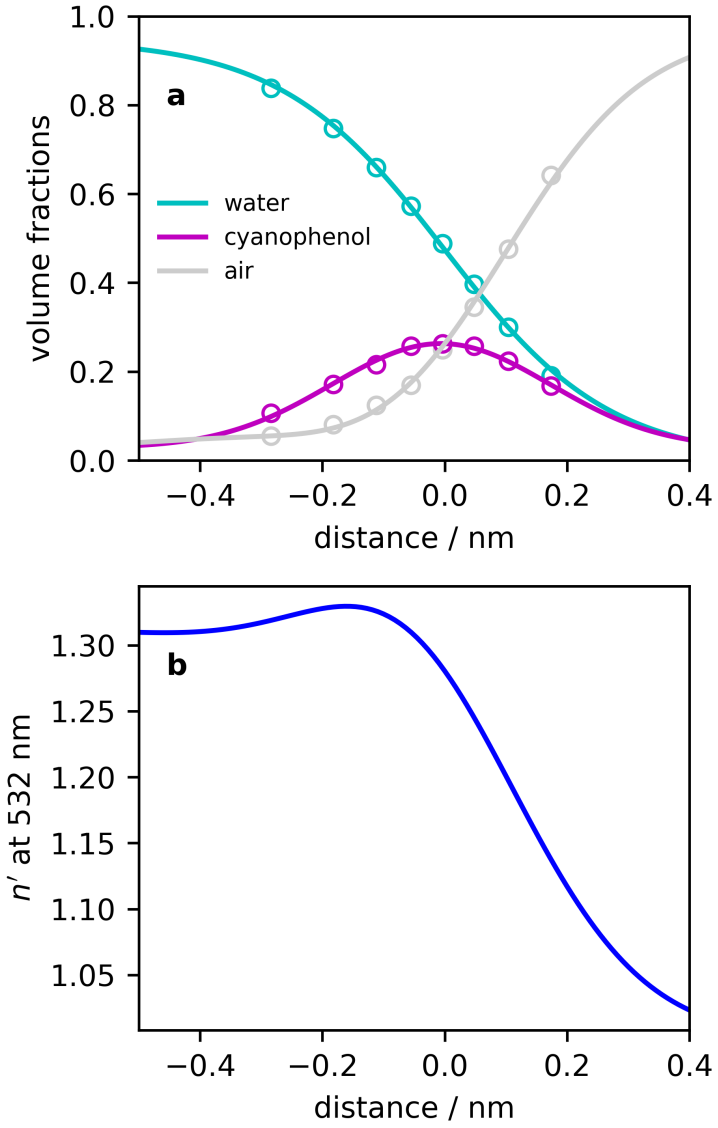

Figure 4.3: (a) Volume fractions of cyanophenol f_{CP}, water f_{W} and air $1 - f_{\mathrm{CP}} - f_{\mathrm{W}}$ as a function of distance across the interface, determined from MD data plotted in points. Here the bulk aqueous phase exists at $z = -\infty$ and $z = 0$ is the Gibbs dividing surface. (b) Distance dependence of n' at 532 nm calculated from Eq. 4.7 using these volume fractions. Reprinted with permission. Copyright 2024 AIP Publishing.

to account for the IR absorption of cyanophenol in the vicinity of the C–N resonance. Fig. 4.3b shows the distance dependence of n' at 532 nm, which has a very similar shape to that at the SFG wavelengths, but $n'(z, \omega_{\mathrm{IR}})$ is also obtained using this approach, enabling the evaluation of $L_{zz}(z)$. The shape of n' in the visible region roughly follows the volume fraction distribution of water across the interface, but with a slight peak close to the Gibbs dividing surface that results from the higher refractive index of p-cyanophenol.

4.3 Orientation parameters

For each z bin, we have analyzed the distribution of C–N bond vectors. Three distributions obtained at different depths in the interfacial region are shown in Fig. 4.4a. Here we can see that the cyanophenol C–N bond axis is fairly broadly tilted at the air–aqueous interface, with an average angle of approximately 75°. This means that a significant fraction of the cyano groups are directed to the bulk aqueous phase, with a slightly greater number pointing towards air ($\theta < 90°$ in our coordinate system). This may be due to competing hydrogen bonding opportunities for C–N and O–H groups. As these moieties are situated in a para configuration, the polarity of the orientation of the whole molecule results from the relative strength of these two types of interactions with bulk water. We then computed the values of $\langle \cos\theta \rangle$ and $\langle \cos^3\theta \rangle$ as shown in Fig. 4.3b. Their positive values are consistent with the fact that the C-to-N vector is predominantly in the first quadrant, i.e. the cyano group points up into the vapor phase and the O–H group at the para position points down into the bulk aqueous phase. It is interesting to note that while $\langle \cos\theta \rangle$ increases towards the vapor phase indicating that the cyano groups are more ordered in environments with less water, $\langle \cos^3\theta \rangle$ remains roughly constant throughout the interfacial region.

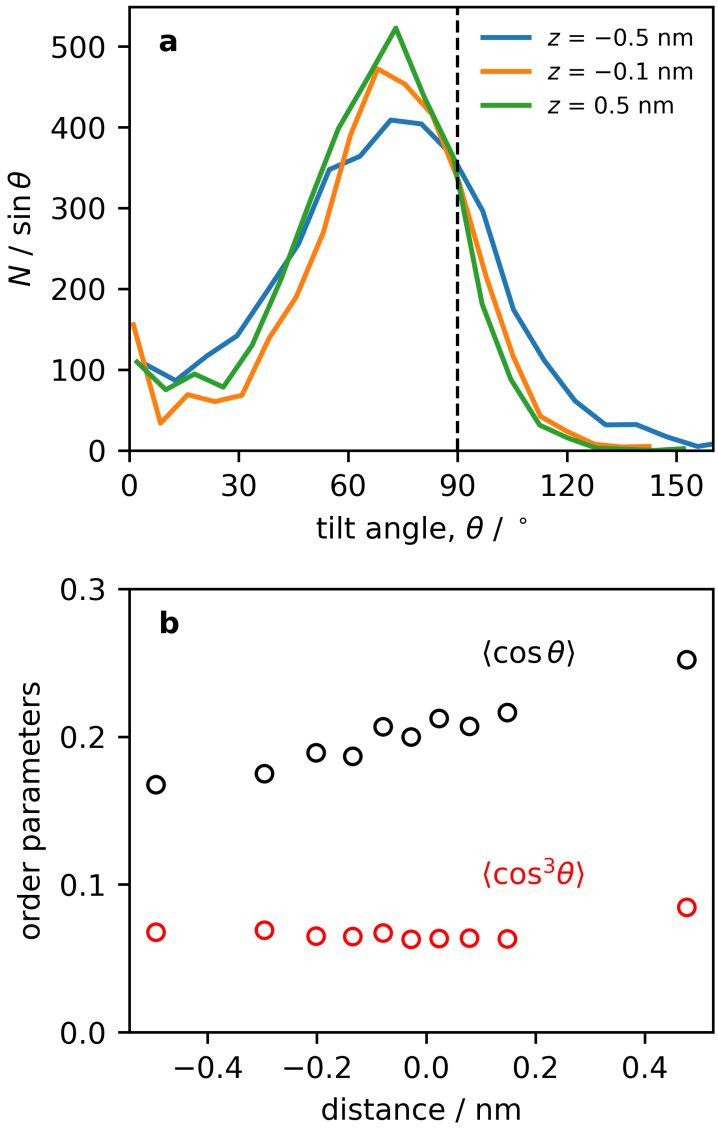

Figure 4.4: (a) Distributions of cyano group tilt angles at depths of $z = -0.5$ nm (towards the bulk aqueous phase, blue), the Gibbs dividing surface (our definition of $z = 0$, shown in orange), and $z = 0.5$ nm (on the vapor side of the interface, green). (b) Values of $\langle \cos\theta \rangle$ (black) and $\langle \cos^3\theta \rangle$ (red) as a function of distance across the interface. Reprinted with permission. Copyright 2024 AIP Publishing.

4.4 SFG response

For the cyano C–N stretching mode with local $C_{\infty v}$ symmetry, one can simplify the hyperpolarizability tensor by defining $R = \alpha^{(2)}_{aac}/\alpha^{(2)}_{ccc}$ to arrive at [9]

$$\chi^{(2)}_{xxz} = \frac{N}{2\varepsilon_0}\alpha^{(2)}_{ccc}\left[(1+R)\langle\cos\theta\rangle - (1-R)\langle\cos^3\theta\rangle\right] \tag{4.8a}$$

$$\chi^{(2)}_{xzx} = \frac{N}{2\varepsilon_0}\alpha^{(2)}_{ccc}(1-R)\left[\langle\cos\theta\rangle - \langle\cos^2\theta\rangle\right] \tag{4.8b}$$

$$\chi^{(2)}_{zzz} = \frac{N}{\varepsilon_0}\alpha^{(2)}_{ccc}\left[R\langle\cos\theta\rangle + (1-R)\langle\cos^3\theta\rangle\right]. \tag{4.8c}$$

However, the results presented in Fig. 4.4b reveal that $\langle\cos\theta\rangle \approx 3\langle\cos^3\theta\rangle$. This has interesting consequences for the subsequent analysis, as Eqs. 4.8a and 4.8b are then equivalent to each other and become

$$\chi^{(2)}_{xxz} = \chi^{(2)}_{zzz} \approx \frac{N}{2\varepsilon_0}\alpha^{(2)}_{ccc}(2R+1)\langle\cos^3\theta\rangle. \tag{4.9}$$

Furthermore, for the set of beam angles used in this experiment, $(L_{xx})_{\mathrm{SFG}}(L_{zz})_{\mathrm{vis}}(L_{xx})_{\mathrm{IR}} \approx -(L_{zz})_{\mathrm{SFG}}(L_{xx})_{\mathrm{vis}}(L_{xx})_{\mathrm{IR}}$ [28]. Together with the fact that $\chi^{(2)}_{xzx} = \chi^{(2)}_{zxx}$ far from electronic resonance, this has the consequence that the PPP spectrum depends only on $\chi^{(2)}_{zxx}$ and $\chi^{(2)}_{zxx}$, which have the same dependence on R and $\langle\cos^3\theta\rangle$ as stated in Eq. 4.9.

The further consequence of this is that the PPP amplitude, when normalized with respect to the SSP amplitude (data shown in Fig. 4.5) is nearly independent of R and the orientation distribution. This means that, when performing the PPP fitting in this way, $\chi^{(2)}_{\mathrm{eff,PPP}}$ depends only on the L factors. We make use of this happy accident to explore the sensitivity of the distance-dependence of n' to capturing the normalized PPP intensity profile. This is done by varying the number of discrete regions over which the volume fraction of the species are characterized for use in Eq. 4.7. We can see that the fit to the data improves as the number of bins increases (Fig. 4.4b), with no significant improvement after the nanometer-sized region is divided into 10 bins. Here we reiterate that there is no difference to the net $\boldsymbol{\chi}^{(2)}$ response whether it is all considered together in the orientation average, or divided into distinct regions, but this illustrates that $\boldsymbol{\chi}^{(2)}_{\mathrm{eff}}(z)$ since $L_{zz}(z)$ through

$n'(z)$. In other words, agreement with the experimental data (standard deviation shown within the grey shaded region) requires that the distance-dependence of n' is considered. It is curious that a single value of n' (1 bin) has nearly the same fit as dividing the interface roughly in half (2 bins). This is likely due to the mismatch between where the cyanophenol molecules are located (as seen in Fig. 4.3a and the overall volume of the interfacial region when only two bins are considered. In this case, one of the regions is predominantly air, with a low refractive index and therefore a large contribution to L_{zz} and $\chi^{(2)}_{\text{eff}}$.

Moving forward with a 10-bin model that describes the interface, we explore whether a small change in the distribution of cyanophenol molecules from that predicted by the MD simulations might provide an even closer match to the experimental results. We start by noting that, since the cyanophenol distribution appears nearly Gaussian in Fig. 4.3b, it can be fit to

$$f_{\text{CP}} = A_{\text{CP}} \exp\left[-\frac{(z-z_0)^2}{2\Gamma_{\text{CP}}^2}\right] + b_{\text{CP}} \tag{4.10}$$

where A_{CP} is the amplitude, z_0 is the position, Γ_{CP} is the width, and b_{CP} is an offset. This result is plotted with the solid purple line in Fig. 4.3a. It is interesting to note that the surfactant distribution is centered at the Gibbs dividing surface ($z_0 \approx 0$), indicating that roughly half of the surface population of the organic species is in a more water-like environment, while half is in a more hydrophobic environment. From this point we chose to keep the water distribution fixed to the profile shown in Fig. 4.3a, but vary the amplitude A and width Γ of the cyanophenol distribution in such a way that the total of the water, organic and air volume fractions does not exceed unity. These results are shown in Fig. 4.6, where the colors correspond to the error associated with the corresponding fits to the normalized PPP spectra. The values of A and Γ obtained by fitting the MD simulation data (purple curve in Fig. 4.3a) produce the result indicated by the red dot. Changing A and Γ in a manner that maintains the same overall surfactant surface number density results in points along the solid red contour. All points above this contour represent distributions with more surfactant molecules at the surface; points below the contour have less molecules present. When both

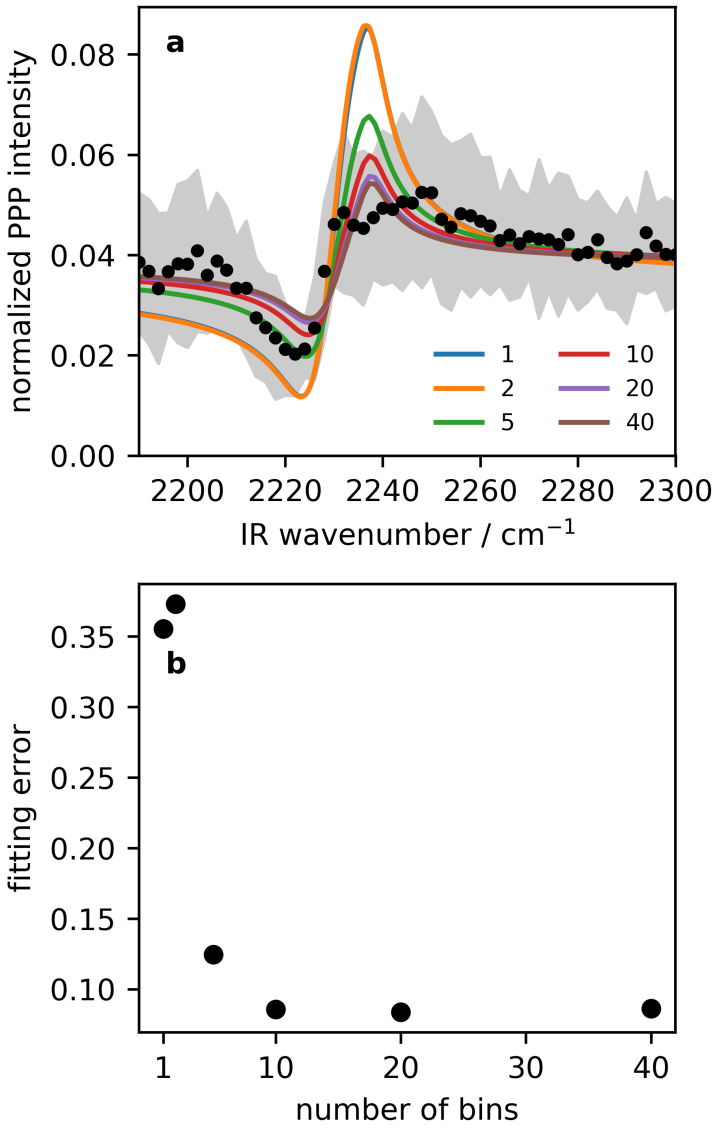

Figure 4.5: (a) Fits to the experimental PPP data when the interface is divided into a varying number of regions for the consideration of local refractive index variation to evaluate n'. (b) The corresponding fitting errors from the sum of squares of the residuals as a function of the number of divisions across the interfacial region. Reprinted with permission. Copyright 2024 AIP Publishing.

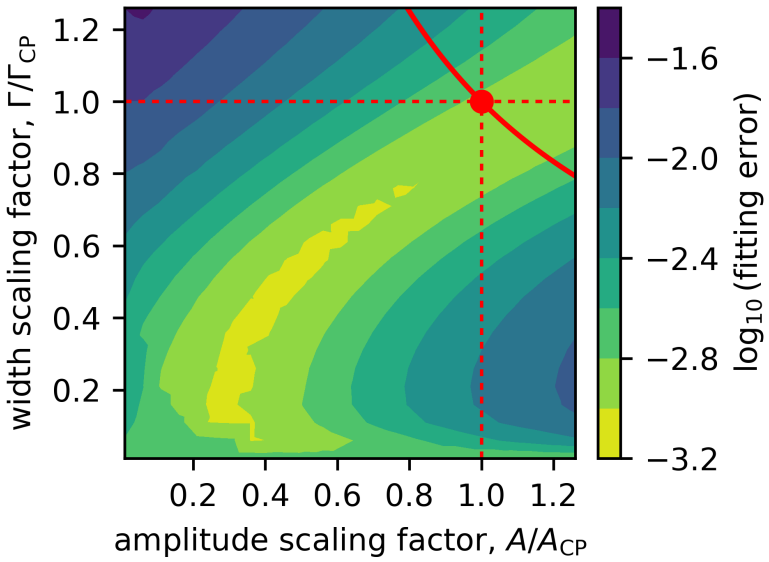

Figure 4.6: Fit to the (SSP-normalized) PPP data for various cyanophenol distributions that are scaled with respect to the MD distribution shown in Fig. 4.3a, according to the amplitude A and width Γ of a Gaussian distribution defined in Eq. 4.10. Reprinted with permission. Copyright 2024 AIP Publishing.

the amplitude and width of the surfactant distribution are decreased, a slightly better fit can be produced. This indicates that the real experimental system may have less molecules adsorbed at the surface compared to what is predicted by the simulations. However, the point corresponding to the direct simulation result produces a fit to the experimental data that is very close to the region of the global minimum. Overall, these results demonstrate that a remarkable agreement between experiment and simulation may be achieved using the relative volume fractions as a function of distance across the interface to determine the local field corrections.

4.5 Conclusion

We have described the necessity of the depth dependence to the overall SFG response. The depth dependence of n' was evaluated using volume fractions taken from classical molecular dynamics and the Lorentz-Lorenz mixing model. The dielectric profile was found to roughly match the profile of water; however, with a slight peak due to the higher

refractive index of cyanophenol. A 10 bin model was deemed sufficient to describe the depth distribution of $\boldsymbol{\chi}^{(2)}_{\text{eff}}$, where less than 10 did not match the experimental data. The cyanophenol molecules were found to orient more strongly closer to the vapor phase. We can also consider it to be likely that the number density is lower than predictions made from surface tension measurements; although, a cyanophenol contribution to n' is still required for proper fit to the experimental data.

Chapter 5

Hyperpolarizibility analysis[1]

5.1 Introduction

In the previous chapter we discussed the relationship between the linear optical proprieties of the interfacial region and the general structure of said interface, now we are interested in the electronic structure of our resonant species. In $\boldsymbol{\chi}^{(2)}$ spectroscopy this molecular property is referred to as the hyperpolarizibility $\boldsymbol{\alpha}^{(2)}$. SFG is similar to other forms of spectroscopy in the sense that understanding the molecular symmetry is required for a complete description of the overall response. For example in the case of the C–N mode of 4-cyanophenol, it is (in solution) impossible to isolate the twist of the benzene ring with respect to the interface; a direct consequence of the $C_{\infty v}$ symmetry. In our previous work [28] we looked to measure the hyperpolarizibility ratio, defined as

$$R = \frac{\alpha^{(2)}_{aac}}{\alpha^{(2)}_{ccc}} = \frac{\alpha'_{aa}}{\alpha'_{cc}}. \tag{5.1}$$

However by examining Fig. 4.2, one can see that we were left with a relatively large range of possibilities, from around $R = 0.08$ to $R = 0.16$. To combat this problem we took advantage of our knowledge of the orientational parameters calculated from classical molecular dynamics, which led to Fig. 5.1. Unfortunately, as noted in the previous chapter the fit from molecular dynamics in the one bin model is far from the global minimum

[1] Reproduced in part from Yang, P.; Kumarasiri, A.; Hore, D.K. "Surface Populations as a Model for the Distance-Dependence of the Interfacial Refractive Index" *J. Chem. Phys.*, **161** 054703 (2024) Copyright 2024 AIP Publishing.

expected from our orientational parameters in Fig. 5.1. In Ref. [28] we took advantage of symmetrical relationships to derive a linear relation between $\chi^{(2)}_{yyz}$, $\chi^{(2)}_{yzy}$, and $\chi^{(2)}_{zzz}$. Now we seek to expand upon our previous work to not only narrow the possible range of the hyperpolarizibility ratio, and generalize our previous linear relationship; but to also create the framework for future direct measurement of R, and use calculated *ab initio* Raman spectra to determine the anisotropy between the bulk and interfacial hyperpolarizibility.

5.2 Determining the hyperpolarizability ratio from SFG data

5.2.1 Symmetry relationships

We recently provided an expression that enables R to be obtained from experimental SFG spectra in a manner that does not require knowledge of the molecular orientation distribution. [28]. Here we first describe how this comes about, and present a slightly more general expression with broader applicability. If we limit the discussion to SFG that is far from electronic resonance, then the Raman tensor is symmetric. We use l,m,n to be any of the molecular frame a,b,c Cartesian components. Using the notation $\alpha'_{lm} \equiv \mathrm{d}\alpha^{(1)}_{lm}/\mathrm{d}Q$ where Q is the normal mode coordinate, the off-resonance condition implies that $\alpha'_{lm} = \alpha'_{ml}$. Similarly, we can define $\mu'_n \equiv \mathrm{d}\mu_n/\mathrm{d}Q$ for the nth component of the dipole moment derivative. This enables all 27 elements of the rank-3 $\boldsymbol{\alpha}^{(2)}$ tensor to be defined using

$$\alpha^{(2)} \propto \begin{bmatrix} \alpha'_{aa} & \alpha'_{ab} & \alpha'_{ac} \\ \alpha'_{ab} & \alpha'_{bb} & \alpha'_{bc} \\ \alpha'_{ac} & \alpha'_{bc} & \alpha'_{cc} \end{bmatrix} \otimes \begin{bmatrix} \mu'_a \\ \mu'_b \\ \mu'_c \end{bmatrix} \tag{5.2}$$

where only 18 of them are unique as a result of the $\boldsymbol{\alpha}'$ symmetry. We next transform all elements of $\boldsymbol{\alpha}^{(2)}$ into the laboratory frame, where the surface is in the xy-plane and z is the surface normal and (i,j,k) serve as placeholders. This operation requires successive applications of the direction cosine matrices that introduce the Euler angles, as described previously, [56] resulting in $\alpha^{(2)}_{ijk}(\theta,\phi,\psi)$.

We now focus on the applications where there is rotational symmetry about the surface

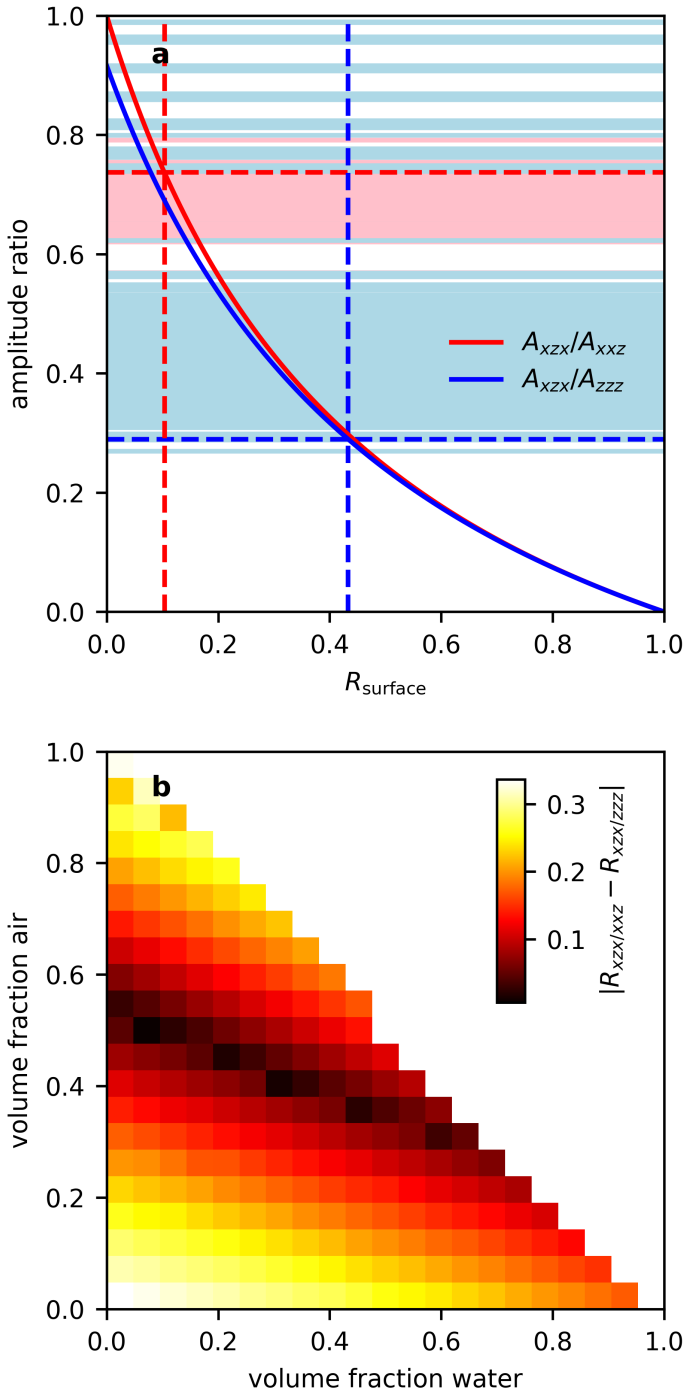

Figure 5.1: (a) Plots of A_{xzx}/A_{xxz} (red curve) and A_{xzx}/A_{zzz} (blue) curve as a function of R_{surface} using values of $\langle \cos\theta \rangle$ and $\langle \cos^3\theta \rangle$ from MD simulations. Intersections with experimentally determined amplitude ratios are shown with the pale red and blue bands for all combinations, and with dashed lines for a particular combination. (b) The difference between the two solutions for R_{surface} obtained in this analysis is plotted as a function of the volume fractions used to approximate n'. Reprinted with permission from Ref. 28. Copyright 2023 American Chemical Society.

normal z (implying a uniform distribution of ϕ), and an isotropic distribution about the molecular c axis, described an integration about ψ.

$$\chi^{(2)}_{ijk}(\theta) = \frac{N}{4\pi^2\varepsilon_0}\int_0^{2\pi}\int_0^{2\pi}\alpha^{(2)}_{ijk}(\theta,\phi,\psi)\,\mathrm{d}\psi\,\mathrm{d}\phi \tag{5.3}$$

This results in 7 non-zero achiral (excluding $\chi^{(2)}_{ijk}$ where $i \neq j \neq k$) elements of $\boldsymbol{\chi}^{(2)}$, of which 3 appear to be unique.

$$\chi^{(2)}_{xxz} = \chi^{(2)}_{yyz} = \frac{N}{4\varepsilon_0}\left[\left(-2\alpha^{(2)}_{aca} - 2\alpha^{(2)}_{bcb} + 2\alpha^{(2)}_{ccc} + \alpha^{(2)}_{aac} + \alpha^{(2)}_{bbc}\right)\langle\cos\theta\rangle\right. \tag{5.4a}$$
$$\left. + \left(2\alpha^{(2)}_{aca} + 2\alpha^{(2)}_{bcb} - 2\alpha^{(2)}_{ccc} + \alpha^{(2)}_{aac} + \alpha^{(2)}_{bbc}\right)\langle\cos^3\theta\rangle\right]$$

$$\chi^{(2)}_{xzx} = \chi^{(2)}_{zxx} = \chi^{(2)}_{yzy} = \chi^{(2)}_{zyy} = \frac{N}{4\varepsilon_0}\left[\left(2\alpha^{(2)}_{ccc} - \alpha^{(2)}_{aac} - \alpha^{(2)}_{bbc}\right)\langle\cos\theta\rangle\right. \tag{5.4b}$$
$$\left. + \left(2\alpha^{(2)}_{aca} + 2\alpha^{(2)}_{bcb} - 2\alpha^{(2)}_{ccc} + \alpha^{(2)}_{bbc} + \alpha^{(2)}_{aac}\right)\langle\cos^3\theta\rangle\right]$$

$$\chi^{(2)}_{zzz} = \frac{N}{2\varepsilon_0}\left[\left(2\alpha^{(2)}_{aca} + 2\alpha^{(2)}_{bcb} + \alpha^{(2)}_{aac} + \alpha^{(2)}_{bbc}\right)\langle\cos\theta\rangle\right. \tag{5.4c}$$
$$\left. - \left(2\alpha^{(2)}_{aca} + 2\alpha^{(2)}_{bcb} - 2\alpha^{(2)}_{ccc} + \alpha^{(2)}_{aac} + \alpha^{(2)}_{bbc}\right)\langle\cos^3\theta\rangle\right].$$

Eqs. 5.4 reveals that, of the 18 elements of $\boldsymbol{\alpha}^{(2)}$ that we initially considered, only $\alpha^{(2)}_{aac}$, $\alpha^{(2)}_{bbc}$, $\alpha^{(2)}_{ccc}$, $\alpha^{(2)}_{aac}$, and $\alpha^{(2)}_{aac}$ contribute to the $\boldsymbol{\chi}^{(2)}$ elements of interest when the orientation distribution is isotropic about ϕ and ψ.

We have then found a linear relationship between these three $\boldsymbol{\chi}^{(2)}$ elements that can be expressed as

$$\chi^{(2)}_{zzz} = c_1\chi^{(2)}_{xxz} + c_2\chi^{(2)}_{xzx} \tag{5.5}$$

where the coefficients c_1 and c_2 were determined to be

$$c_1 = -2\left(\frac{\alpha^{(2)}_{aca} + \alpha^{(2)}_{bcb} + \alpha^{(2)}_{ccc}}{\alpha^{(2)}_{aca} - \alpha^{(2)}_{aac} + \alpha^{(2)}_{bcb} - \alpha^{(2)}_{bbc}}\right) \tag{5.6a}$$

$$c_2 = 2\left(\frac{\alpha^{(2)}_{aac} + \alpha^{(2)}_{bbc} + \alpha^{(2)}_{ccc}}{\alpha^{(2)}_{aca} - \alpha^{(2)}_{aac} + \alpha^{(2)}_{bcb} - \alpha^{(2)}_{bbc}}\right) \tag{5.6b}$$

which is valid for any symmetry of the molecular hyperpolarizibility $\boldsymbol{\alpha}^{(2)}$, and any distribution of the tilt angle θ.

There are several implications of Eq. 5.5. The first is that the three $\boldsymbol{\chi}^{(2)}$ tensor elements in Eq. 5.4 are in fact not unique. This conclusion also extends to the effective susceptibilities, in that only two of SSP, SPS (or PSS) or PPP polarization schemes are unique. In other words, if any two of these measurements are performed, the third is predictable. Finally, in the analysis of SFG spectra, it is more practical to work with ratios of intensities, or ratios of fit vibrational mode amplitudes. Such ratios serve three functions: they enable an orientation analysis independent of the surface number density N; independent of the absolute magnitude of the molecular hyperpolarizability tensor elements $\alpha^{(2)}_{lmn}$; and does not necessitate measuring $\chi^{(2)}_{ijk}$ to absolute units. The ramification of this is that, with only two of $\chi^{(2)}_{xxz}$, $\chi^{(2)}_{xzx}$ or $\chi^{(2)}_{zzz}$ unique, only one unique ratio can be formed.

The final impact is that, in the case of such symmetry about z and c, it is not possible to isolate $\langle\cos\theta\rangle$ and $\langle\cos^3\theta\rangle$, and only the ratio $\langle\cos\theta\rangle/\langle\cos^3\theta\rangle$ may be determined. Some further discussion about the implications of being restricted to the knowledge of the $\langle\cos\theta\rangle/\langle\cos^3\theta\rangle$ ratio, without explicit access to $\langle P_1\rangle$ and $\langle P_3\rangle$, can be found in Ref. 9.

We note that the coefficients c_1 and c_2 in Eq. 5.5 are independent of any orientation parameters. This has an additional benefit when we return to our specific case of the cyano C–N stretch where $\alpha^{(2)}_{aac} = \alpha^{(2)}_{bbc}$ and $\alpha^{(2)}_{ccc}$ are the only three non-zero hyperpolarizability tensor elements. In this case, Eqs. 5.4 become Eqs. 4.8, and the coefficients appearing in Eq. 5.5 simplify to

$$c_1 = \frac{\alpha^{(2)}_{ccc}}{\alpha^{(2)}_{aac}} = \frac{1}{R} \tag{5.7a}$$

$$c_2 = -\left(\frac{2\alpha^{(2)}_{aac} + \alpha^{(2)}_{ccc}}{\alpha^{(2)}_{aac}}\right) = -\left(2 + \frac{1}{R}\right). \tag{5.7b}$$

In the SFG literature, this quantity is typically referred to simply as R, but we use the explicit notation R to illustrate that this is related to the electronic structure of the molecules at the surface. Since Eq. 5.2 illustrates that $\alpha^{(2)}_{lmn}$ is proportional to $\alpha'_{lm}\mu'_n$, we can see that $R = \alpha'_{aa}/\alpha'_{cc}$ as the factors of μ'_c cancel. However, we make the distinction between this and the bulk material or solution-phase quantity $R_{\mathrm{B}} = \alpha'_{aa}/\alpha'_{cc}$ (that can be obtained from

the Raman depolarization ratio) as the electronic structure may be perturbed at the interface for a variety of reasons.

A final consequence of Eq. 5.5 is that no assumptions about the orientation distribution need to be made, since $\langle\cos\theta\rangle$ and $\langle\cos^3\theta\rangle$ do not appear in the coefficients in Eqs. 5.6. In the case of our high-symmetry modes characterized by R, this further enables us to write

$$R = \frac{\chi^{(2)}_{xxz} - \chi^{(2)}_{xzx}}{\chi^{(2)}_{zzz} + 2\chi^{(2)}_{xzx}} \tag{5.8}$$

as we have recently demonstrated [28]. Similar relationships exist for local modes with other symmetries [57] that lead to additional possibilities for orientation-insensitive measurements [58, 59].

5.2.2 SPS spectra

Now that a suitable model for $n'(z)$ has been established from the PPP data using 10 bins, this can be applied to the analysis of the (SSP-normalized) SPS data. In this case, our situation of $\langle\cos\theta\rangle \approx 3\langle\cos^3\theta\rangle$ leads to

$$\chi^{(2)}_{xzx} \approx \frac{N}{2\varepsilon_0}\alpha^{(2)}_{ccc}(1-R)\langle\cos^3\theta\rangle \tag{5.9}$$

where we can see that the SPS to SSP (given by $\chi^{(2)}_{xxz}$ in Eq. 4.9) ratio is expected to be sensitive to R. This is indeed the case, as can be seen in Fig. 5.2. Fitting to the experimental data identifies the optimal value of $R = 0.13 \pm 0.03$. This value is within the range of $R_{\mathrm{B}} < R < 2R_{\mathrm{B}}$ that we have established previously [28], but now confined to a slightly more narrow range.

5.3 Additional possibilities from polarization null angle experiments

Here we describe a possible method to calculate the hyperpolarizability ratio R without the assumption of any lineshape or the fitting of any spectra. We will be assuming that this

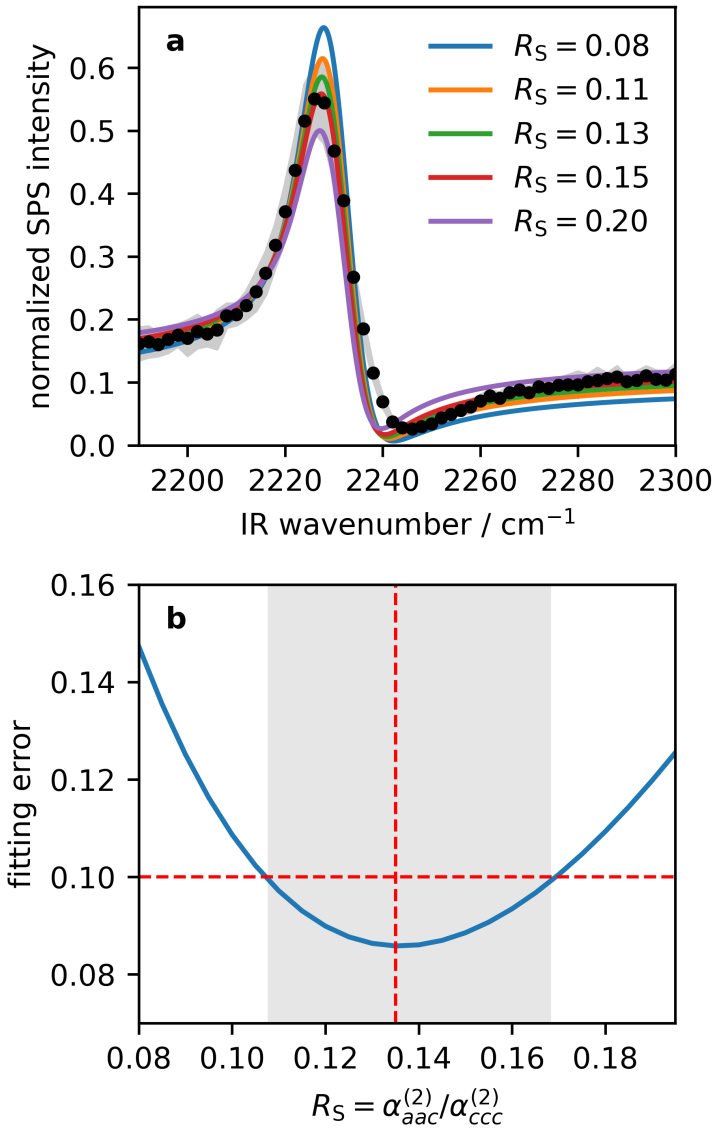

Figure 5.2: (a) Fitting the SPS data with different values of R ranging from $R = R_B = 0.08$ to $R = 0.2$. Experimental data is plotted in points, and the range of one standard deviation about the mean is highlighted in grey. (b) The quality of the fit to the experimental data as determined by the sum of the squares of the residuals, highlighting the best fit result obtained $R = 0.13$. Reprinted with permission. Copyright 2024 AIP Publishing.

experiment is heterodyned, (which is a technique that gives isolated access to the real and imaginary components of the $\boldsymbol{\chi}^{(2)}$ response). Then we can write $\boldsymbol{\chi}^{(2)}_{\text{eff}}$ as

$$\begin{aligned}\chi^{(2)}_{\text{eff}} &= \sin(\Omega)\sin(\Omega_1)\cos(\Omega_2)\chi^{(2)}_{\text{eff,ssp}} \\ &+ \sin(\Omega)\cos(\Omega_1)\sin(\Omega_2)\chi^{(2)}_{\text{eff,sps}} \\ &+ \cos(\Omega)\sin(\Omega_1)\sin(\Omega_2)\chi^{(2)}_{\text{eff,pss}} \\ &+ \cos(\Omega)\cos(\Omega_1)\cos(\Omega_2)\chi^{(2)}_{\text{eff,ppp}}\end{aligned} \tag{5.10}$$

Here we define Ω to be the polarizer angle, where Ω refers to the SFG polarizer, Ω_1 the visible and, Ω_2 the IR. By convention 0° is defined to be P polarized and 90° polarized. Then by setting Ω to 90° (or S) and Ω_2 to -45° we arrive at

$$\chi^{(2)}_{\text{eff}} = \frac{-\sqrt{2}}{2}\sin(\Omega_1)\chi^{(2)}_{\text{eff,ssp}} + \frac{\sqrt{2}}{2}\cos(\Omega_1)\chi^{(2)}_{\text{eff,sps}} \tag{5.11}$$

Then by finding Ω_1 where there is zero SFG response, we get

$$\tan(\Omega_1') = \frac{\chi^{(2)}_{xzx}LLL_{yzy}}{\chi^{(2)}_{xxz}LLL_{yyz}} \tag{5.12}$$

Up to here the PNA method was described in detail by Ref [9], but now we use the previous assumption of a hetrodyne experiment to only probe the imaginary component of $\boldsymbol{\chi}^{(2)}$, this allows for the removal of the non-resonant component as we are assuming it to be completely real. Then we can replace $\boldsymbol{\chi}^{(2)}$ in Eq. 5.12 with the resonant amplitude to arrive at the relationship

$$\tan(\Omega_1') = \frac{A_{xzx}LLL_{yzy}}{A_{xxz}LLL_{yyz}} \tag{5.13}$$

In the same way as Eq. 5.11 by setting $\Omega_2 = 0$ or (P) and $\Omega = -45^\circ$ we can arrive at

$$\tan(\Omega_1'') = \frac{-A_{xxz}LLL_{xxz} - A_{xzx}LLL_{xzx} + A_{xzx}LLL_{zxx} + A_{zzz}LLL_{zzz}}{A_{xxz}LLL_{yyz}}. \tag{5.14}$$

Then by taking advantage of the previous equation

$$\begin{aligned}\tan(\Omega_1'') &= -\frac{LLL_{xxz}}{LLL_{yyz}} - \tan(\Omega_1')LLL_{xxz}LLL_{yzy} \\ &+ \tan(\Omega_1')LLL_{zxx}LLL_{yzy} + \frac{A_{zzz}LLL_{zzz}}{A_{xxz}LLL_{yyz}}\end{aligned} \tag{5.15}$$

$$\frac{A_{zzz}}{A_{xxz}} = \frac{LLL_{yyz}}{LLL_{zzz}}\left(\tan(\Omega_1'') - \frac{LLL_{xxz}}{LLL_{yyz}} - \tan(\Omega_1')LLL_{xxz}LLL_{yzy} + \tan(\Omega_1')LLL_{zxx}LLL_{yzy}\right). \tag{5.16}$$

Finally by taking advantage of Eq. 5.8 we then find the hyperpolarizibility ratio R

$$R = \frac{1 - \tan(\Omega_1')\frac{LLL_{yyz}}{LLL_{yzy}}}{\frac{LLL_{yyz}}{LLL_{zzz}}\left[\tan(\Omega_1'') - \frac{LLL_{xxz}}{LLL_{yyz}} - \tan(\Omega_1')LLL_{xxz}LLL_{yzy} + \tan(\Omega_1')LLL_{zxx}LLL_{yzy}\right] + 2\tan(\Omega_1')\frac{LLL_{yyz}}{LLL_{yzy}}}. \tag{5.17}$$

One should note that this method still contends with the challenges of the local field correction. In spite of that challenge our method allows for a more accurate measurement of the amplitude ratios and therefore R, given that one should be able to measure Ω', Ω'' to within 1°. Another somewhat obfuscated benefit would be the lack of the requirement for any calibration; in normal measurements one must take the ratio of two different polarization combinations, where such a ratio must be calibrated against a known standard such as quartz to ensure no issues arising from changes in beam overlap for example. This is made unnecessary in such a PNA measurement due to the fact that the rotation causes zero signal where calibration would be meaningless. This is a benefit in even the more traditional homodyne based approach as discovered by Wang *et al* [9, 60, 61]. Given that a hetrodyne measurement is quite challenging experimentally, it could also be possible to use the maximum entropy method to calculate the imaginary spectrum [62]; however MEM cannot distinguish the sign of the resonant amplitude. This is irrelevant as the signs of the amplitudes, are unnecessary in this case; as we are only interested in the magnitude of the imaginary response.

5.3.1 Calibration of intensity spectra using null angles

Here we give a brief description of a method to correct for the relative experimental ratios of $\boldsymbol{\chi}^{(2)}_{\text{eff}}$; as differences in beam overlap between polarization combinations (and other factors) may cause deviation from the true value when measured. First let us apply a calibration

function to Eq. 5.10

$$\begin{aligned} F(\Omega,\Omega_1,\Omega_2)\chi^{(2)}_{\text{eff}} &= \sin(\Omega)\sin(\Omega_1)\cos(\Omega_2)\chi^{(2)}_{\text{eff,ssp}} \\ &+ \sin(\Omega)\cos(\Omega_1)\sin(\Omega_2)\chi^{(2)}_{\text{eff,sps}} \\ &+ \cos(\Omega)\sin(\Omega_1)\sin(\Omega_2)\chi^{(2)}_{\text{eff,pss}} \\ &+ \cos(\Omega)\cos(\Omega_1)\cos(\Omega_2)\chi^{(2)}_{\text{eff,ppp}}. \end{aligned} \tag{5.18}$$

Where F is a generalized function that accounts for the calibration required from varying polarizer angles. Now given that we can assume F is non-zero everywhere, it is easy to see that if Eq. 5.11 is zero, F no longer has any impact. Therefore one can use ratios taken from Eq. 5.12 to correct the relative difference between the SPS and SSP polarizations; the other polarization combinations can be corrected in the same manner. This greatly simplifies the experimental procedure where calibrating the relative ratios between elements of $\boldsymbol{\chi}^{(2)}_{\text{eff}}$ can be difficult. We do implicitly make the assumption that the calibration function is applied to the overall $\boldsymbol{\chi}^{(2)}_{\text{eff}}$ response; whether this assumption is unfounded is left as an open question.

5.4 Electronic structure calculations

From our static electronic structure calculations we measured a value of $R = 0.047$ for gas-phase 4-cyanophenol; however commonly a value of $R = 0.26$ is given [9, 36]. We can then infer there to be some issue with the standard literature value, given that there should not be such a large discrepancy between the two measurements even taking the inherent challenges of density functional theory calculations. An interesting fact may be from some confusion in nomenclature; frequently the hyperpolarizability ratio is referred to as the depolarization ratio. This is not ideal as confusion can easily propagate as there have been many such Raman measurements of C–N modes depolarization ratios close to 0.26 [63–65]. Furthermore, it is possible to calculate the hyperpolarizibility ratio directly from the Raman depolarization ratio. More discussion will be given in the next section. Of course the naming is not the only source of the aforementioned $R = 0.26$, the main being Ref. 36; a paper (where the slab model for n' is derived) which did give experimental

Molecule	Solvent	Depolarization Ratio ρ	Hyperpolarizability ratio R
4-Cyanophenol	Gas	0.28	0.047
4-Cyanophenol	Water	0.29	0.046
4-Cyanophenol	Benzonitrile	0.30	0.036
Benzonitrile	Water	0.28	0.045
Acetonitrile	Gas	0.15	0.021
Acetonitrile	Water	0.16	0.020

Table 5.1: Hyperpolarizibilities and Raman depolarization ratios calculated by static density functional theory calculations in gas-phase and with implicit solvation models.

evidence for $R = 0.26$. Given the evidence from our static calculations, and our previous SFG based approach [28], we consider it likely incorrect.

Now let us evaluate the data presented in Table 5.1; starting with the gas-phase measurements. We see a difference of a factor of two between the acetonitrile and cyanophenol data. We can rationalize this by assuming there to be some form of stabilization caused by the presence of the phenyl ring. Now if we consider the addition of a PCM solvent we can make some small inferences. In all the molecules evaluated we fail to see much difference in the new dielectric medium. Of course we cannot conclusively claim little difference in the presence of such a solvent because of the inherent limitations of the PCM; although it lends credence to the belief that one should not expect a large difference between interfacial and solvated 4-cyanophenol. The only case where a large change in the hyperpolarizibility ratio is measured is the presence of benzonitrile used a surrogate for cyanophenol; based on the expected surface density of cyanophenol from tension measurements [21] we can assume that every cyanophenol molecule can be more accurately described as being solvated in water, rather than organic solvent. Perhaps in solid phase where we could potentially consider as significantly different based on the benzonitrile solvation; however there is little reason to believe a PCM solvation would translate well to solid phase, especially considering its application to real liquid solvation is questionable. The solution would be to use some form of explicit solvation, likely in the form of an *ab initio* molecular dynamics simulation.

5.5 Conclusion

The range of hyperpolarizibility ratios as established previously [28] was narrowed slightly to $R = 0.13 \pm .03$ by fitting to experimental SPS spectra. We derived a new general linear relationship between $\boldsymbol{\chi}^{(2)}$ elements; this discovery precludes the separation of the order parameters $\langle \cos\theta \rangle$ and $\langle \cos^3\theta \rangle$ in most quantitative SFG measurements. A new direct experimental method for measuring R directly was derived by: expanding previous work in PNA measurements, removing the non-resonant component by using the imaginary response, and the linear relationship between elements of $\boldsymbol{\chi}^{(2)}$.

Chapter 6

Ab initio Molecular Dynamics

6.1 Introduction

While static calculations are frequently used in lieu of an actual experimental measurement of the hyperpolarizibility ratio [38,66–69], there are a few downsides to such a calculation. Importantly most implicit solvation models are likely not sufficient to describe specific hydrogen bonding environment of the interface, or other similar changes in the interfacial environment. However an interesting solution is derived from experimental spontaneous Raman measurements, the depolarization ratio. As mentioned previously it is possible to write the hyperpolarizibility ratio as a function of Raman tensor elements

$$R = \frac{\alpha^{(2)}_{aac}}{\alpha^{(2)}_{ccc}} = \frac{\alpha^{(2)}_{bbc}}{\alpha^{(2)}_{ccc}} = \frac{\alpha'_{aa}}{\alpha'_{cc}} = \frac{\alpha'_{bb}}{\alpha'_{cc}}. \tag{6.1}$$

Then if we also consider the form of the Raman depolarization ratio ρ in the case of c_{3v} (or higher) symmetry [9,28,70]

$$\rho = \frac{3\gamma^2}{45\alpha^2 + 4\gamma^2} = \frac{3}{4 + 5\left[(1+2R)/(R-1)\right]^2} \tag{6.2}$$

where α is the isotropic and γ is the anisotropic contribution. Then if we define

$$Q = \sqrt{(3/5)\left[(1/\rho) - (4/3)\right]} \tag{6.3}$$

we then arrive at

$$R = \pm\frac{Q+1}{Q-2} \tag{6.4}$$

giving two distinct solutions of which one is valid [71]. The determination of which solution can generally be inferred thorough chemical intuition, for example the CH_3 mode where $R > 1$ is well known [36] or C–N where $R < 1$ [28, 36, 71]. The main issue with this approach is due to the $\boldsymbol{\chi}^{(3)}$ nature of spontaneous Raman far from electronic resonance where there is no centrosymmetry breaking requirement as in SFG. This implies that any Raman measurement will in general be dominated by the bulk contribution and may not have necessarily have the same hyperpolarizibility as the interfacial region. The solution is to use *ab initio* molecular dynamics calculations to calculate Raman spectra with a cyanophenol molecule strategically placed in the interfacial region. The Raman response can be written as the Fourier transform of the autocorrelation of the polarizibility over time [72].

$$I(\omega)_{\parallel} = \frac{(\omega_{in} - \omega)^4}{\omega} \frac{1}{1 - \exp(-\hbar\omega/k_b T)} \omega^2 \int \langle \alpha_{xx}(\tau)\alpha_{xx}(\tau + t)\rangle_{\tau} \mathrm{e}^{-i\omega t} dt. \tag{6.5}$$

The depolarization ratio can then be calculated using the above and Eq. 6.2, where the polarizibilities are replaced with the correct Cartesian coordinates and the appropriate Fourier transform. Analogously the IR and SFG spectra can be calculated using the autocorrelation of the dipole-moment and the correlation of the dipole-moment and polarizibility respectively. This has a few main benefits over common computational approaches; the first being the lack of any lineshape function. Frequently when one calculates Raman or IR spectra statically one must also use a lineshape such as a Lorentzian or Voigt, which adds another layer of difficulty in matching experimental data. In this sense we can consider AIMD generated spectra to be completely *ab initio* as we are not applying any frequency scaling or lineshape function. Secondly, especially for bulk systems modeling the actual system thermodynamically in one snapshot is quite challenging (if not impossible) [32]. Both of these problems are solved in the AIMD approach; in our case the main benefit is the accurate modelling of the interfacial and bulk environments.

Previously we have taken depolarization ratio measurements from a bulk solution of p-cyanophenol as shown in Fig. 6.4; we measured a value of $\rho = 0.249 \pm 0.003$ [28]. In

liquid crystal literature many Raman depolarization measurements have been taken of both 4-cyano-4'-pentylbiphenyl (5CB) and 4'-octyl-4-biphenylcarbonitrile (8CB), of which all had values close to $\rho = 0.26$ even under changing pressure and temperature [63–65]. This led to reasoning that most cyano groups should have similar hyperpolarizibility ratios in the bulk and interfacial environments [9]; furthermore, the bulk value is within the range of possibilities expected in our non-depth dependant SFG measurement, and is close to within our standard deviation discussed in Section 5.2. However given that Eq. 6.4 is quite sensitive, even a change of 0.1 in the depolarization ratio would lead to a hyperpolarizability ratio in the middle of what is expected from the depth-dependant approach; we can also assume that it is not likely that cyanophenol has the same bulk depolarization ratio as 5CB and 8CB.

6.2 Orientation and depth distribution

While the depolarization ratio is invariant with respect to the orientation distribution, it can be helpful to probe in order to ensure good convergence of our AIMD trajectory. One would expect a uniform distribution of θ in the bulk case; secondly, the order parameters of the surface simulation should roughy match our previous classical simulations given that the orientational distribution does not change much with increasing surface number density.

From Fig. 6.1, we have the tilt angle distributions, similar to Chapter 3, where we had results from classical simulations. At first one might be confused about the results presented here, given that they are both noisy and do not seem similar to those found above. However, if we consider that the AIMD simulations ran for 80 ps or 0.08 ns (around the time it takes water to diffuse 6 Å), and that the simulation box contains 200 times less cyanophenol molecules, we can ignore some of the differences in accuracy and focus more on the overall shape and trends. In Fig. 6.1a we can see evidence of a somewhat uniform distribution, while in Fig. 6.1b we see evidence of an upwards preference, both as expected based on their bulk and interfacial environments. Furthermore in the case of the

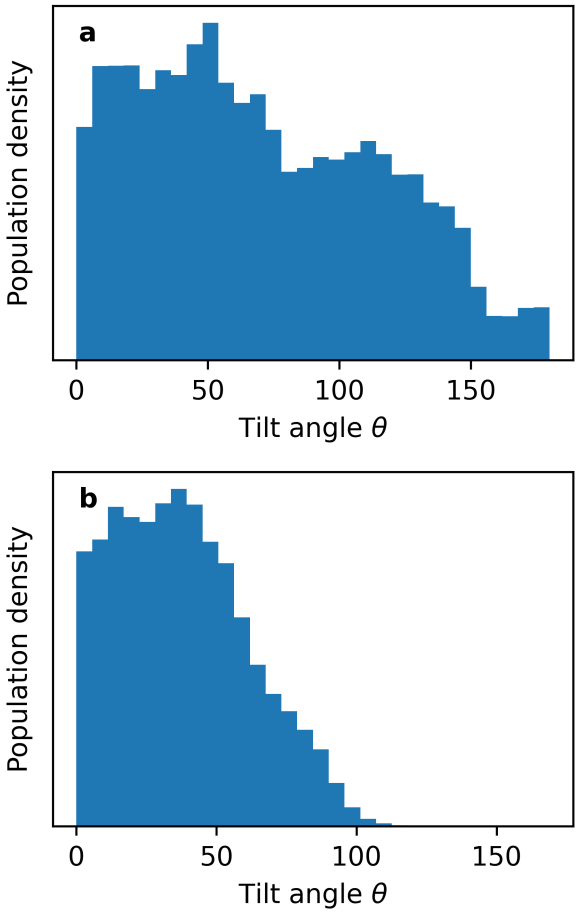

Figure 6.1: (a) Tilt angle histogram of cyanophenol in bulk solution calculated from AIMD. (b) Tilt angle distribution of cyanophenol at the water–vapor interface calculated from AIMD. Both distributions have been $\sin\theta$ corrected.

interfacial distribution, we would expect to see slightly more upwards preference compared to the classical trajectories based on Fig. 6.2 where the average depth of the cyanophenol molecule is higher than the average in the classical simulations; we see similar behavior in Fig. 4.4 where the distribution became more ordered closer to the interface. One way to combat the problem of poor orientation would be to randomly probe different parts of the classical simulation and then run AIMD on those snapshots. This works as there is no requirement for the non-chiral *ab initio* spectra to be in any specific order [73].

If we turn our attention to Fig. 6.2, we can examine the depth distribution of the cyanophenol molecule at the interface. We should note that we have defined 0 to be the highest position of any water molecule in each time step which removes the issue of the trajectory drifting, also given the fact that the simulation is relatively short and the small size; we do not see any water molecules move into the vapor-phase. Over the entire length of the trajectory there does not seem to be any significant time-step where we could consider the cyanophenol molecule to be in bulk-phase; given that at most we see a 5 Ådepth probably caused by the rotation of the cyanophenol molecule instead of its movement into the bulk. Its important to note that the average depth being higher than in the classical simulations is a benefit in the sense that there is an even larger difference between the the surface and bulk systems. We used the C–N bond here instead of the center of mass as we can expect the location of the C–N bond to have the largest impact on whether the chromophore can be considered interfacial.

6.3 Raman spectra from AIMD

We can first compare Fig. 6.3a, and Fig. 6.3b , we see some small differences in the overall relative intensity in the low frequency modes from 500–2000 cm^{-1}, generally trending towards higher intensity overall in the bulk-phase spectra. There could be a few reasons for this, it could be the case that the large box size in the z-direction for the surface spectra causes some loss in the polarizibility. For the cyano-based peaks it could also be from the

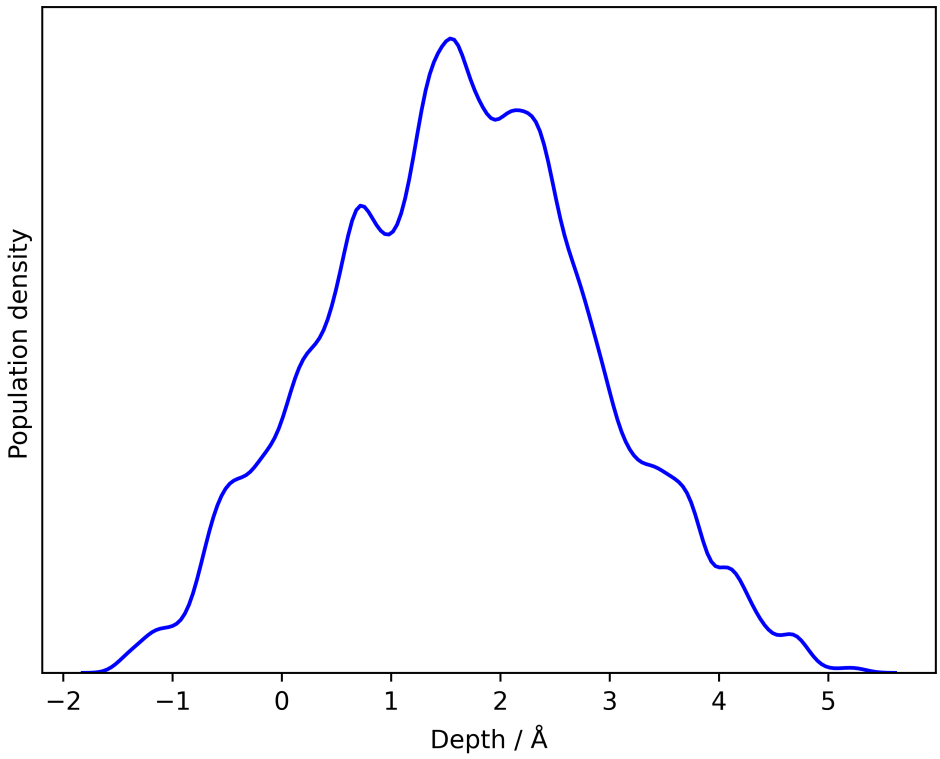

Figure 6.2: Depth distribution of the C–N bond of p-cyanophenol at the water–vapor interface, where 0 is defined to be the highest extent of the water interface.

differences in the orientation distribution. A region of interest where we observe major differences would be the O–H region from 3100–3500 cm^{-1}. One of the most studied regions in SFG spectroscopy is the sharp free-O–H peak generally blueshifted from the common broad peak observed in neat water. We observe this peak in Fig. 6.5a and the isolated water spectra in Fig. 6.6, another indication that our trajectory accurately represents the interfacial region. This is interesting in the sense that such a peak would be invisible in a standard Raman measurement owing to its $\boldsymbol{\chi}^{(3)}$ nature as the bulk signal would overwhelm any surface-active water molecules. It is likely given that the system size of the water-vapor simulation we can consider almost every water molecule to be in some way affected by the interface, as our system is only 2 nm in the $\hat{z}$ direction; the water interface is generally considered to be slightly larger then 1 nm as seen in Fig. 4.3. This certainly

reduces the overall density of the system. There is likely no actual bulk-phase in the surface simulation. If one wanted more representative interfacial water spectra, or even to depth profile the Raman (or IR) response, an idea would be to (with a larger simulation) run the dynamics portion normally, however post-production run re-label the H_2O molecules as a function of depth before the electron density calculation; then it would be simple to split the Raman response however one desires. This could even potentially be done at charged interfaces such as silica-water, where the response from the Stern/diffuse layers could be disentangled.

Now we turn our attention to the specific cyano-stretch region of 2150–2300 cm^{-1} from AIMD in Fig. 6.5, and experimentally in Fig. 6.4. Interestingly even in the experimental data there appears to be some asymmetric broadening, albeit strongest with the interfacial simulation. We find it unlikely to have arisen from any form of solvent interaction given that we observe the effect in the experimental data; this reasoning also precludes any possibility of differences in the chromophore location such as maybe some anisotropy in the dielectric medium. This could be the source of the poor fit we observed in our SFG data in the preceding chapters. We also observe there to be significantly more broadening in our generated spectra compared to experiment, this could be because of the functional or basis set choice; potentially also the probing step size when calculating the electron density. Another point of interest would be the apparent red-shift in our *ab initio* data with respect to the experiment; this expected as frequencies are commonly red-shifted in *ab initio* MD based spectra [72]. Importantly we are not applying any form of scaling factor as is common in static calculations to account for the neglect of anharmonic effects. Furthermore, higher quality frequencies are possible with more computationally expensive functionals in the dynamics portion of generating AIMD spectra [72].

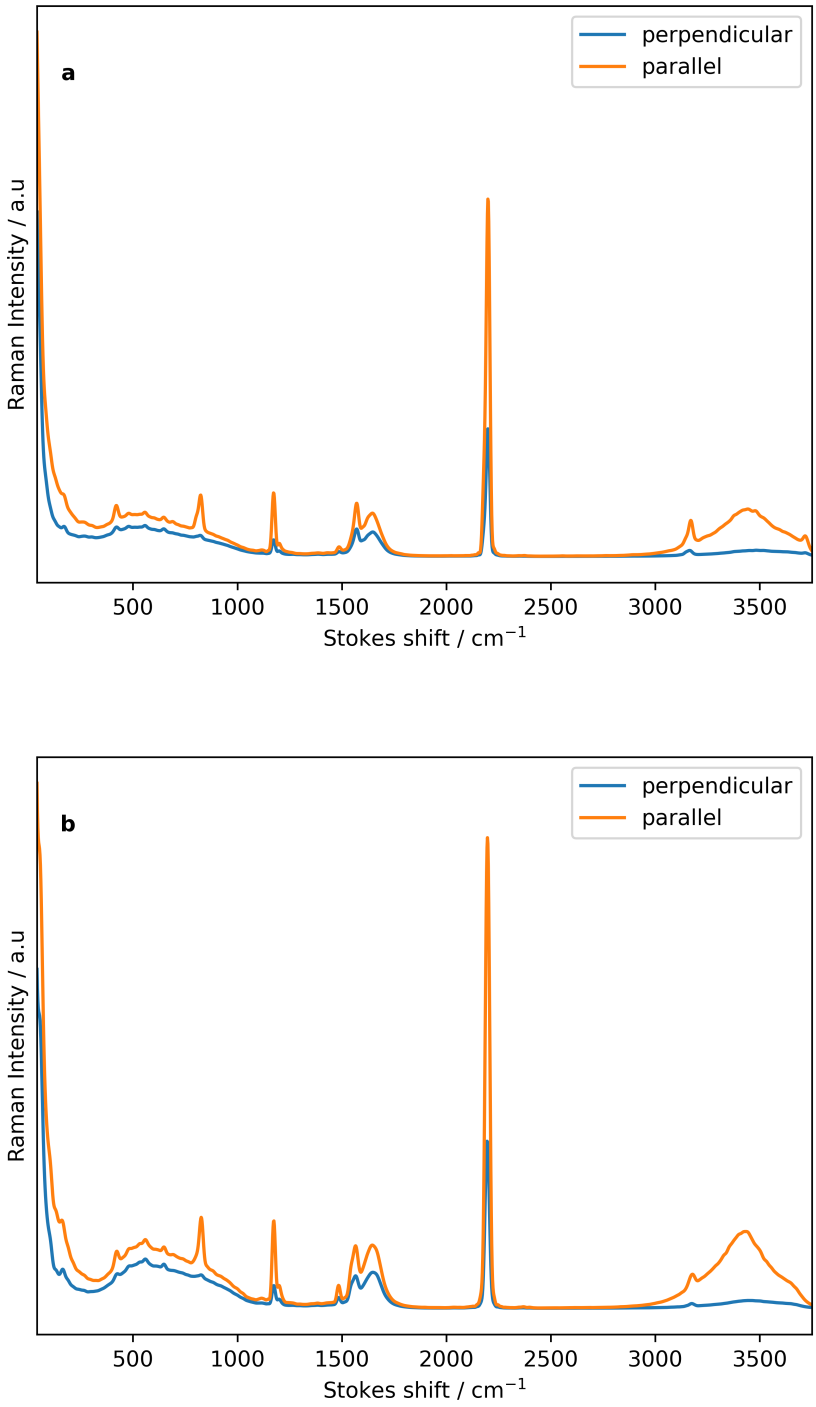

Figure 6.3: (a) Raman spectra generated from *ab initio* molecular dynamics trajectory, at the water–vapor interface with one cyanophenol present. (b) Raman spectra generated from *ab initio* molecular dynamics trajectory, in bulk water with one cyanophenol present.

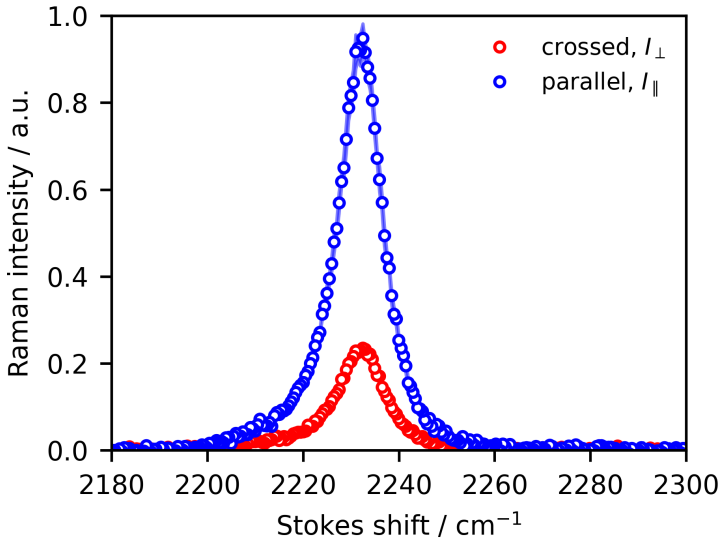

Figure 6.4: Raman spectrum in the range of the C–N mode, both the parallel and perpendicular geometries are shown. Spectra was corrected using known values of carbon tetrachloride. Reprinted with permission from Ref 28. Copyright 2023 American Chemical Society.

6.4 Depolarization ratio

Our main parameter of interest in the Raman depolarization ratio ρ, and by extension the hyperpolarizability ratio R. As discussed previously it was unknown whether bulk measurements could be representative of the true interfacial value. Now from Fig. 6.7, we can calculate $\rho_{\text{surface}} = 0.335$ and $\rho_{\text{bulk}} = 0.312$. These values especially the bulk value do not match our experimental data, most likely due to the limitations caused by functional choice. However, we can still infer that the values for ρ_{bulk} and ρ_{surface} are similar, which is strong evidence that there is no significant change in hyperpolarizibility ratio from bulk to surface modalities. We use ρ instead of R here as in this range R is extremely sensitive to small changes in the depolarization ratio, and the fact that these values carry some form of invisible error which would be magnified in the conversion to the hyperpolarizibility ratio. From these data we can be reasonably confident that bulk-phase Raman measurements should be representative of the true interfacial value. One way to calibrate the magnitude of the depolarization ratio would be to use a liquid of known value and calculate ρ in the

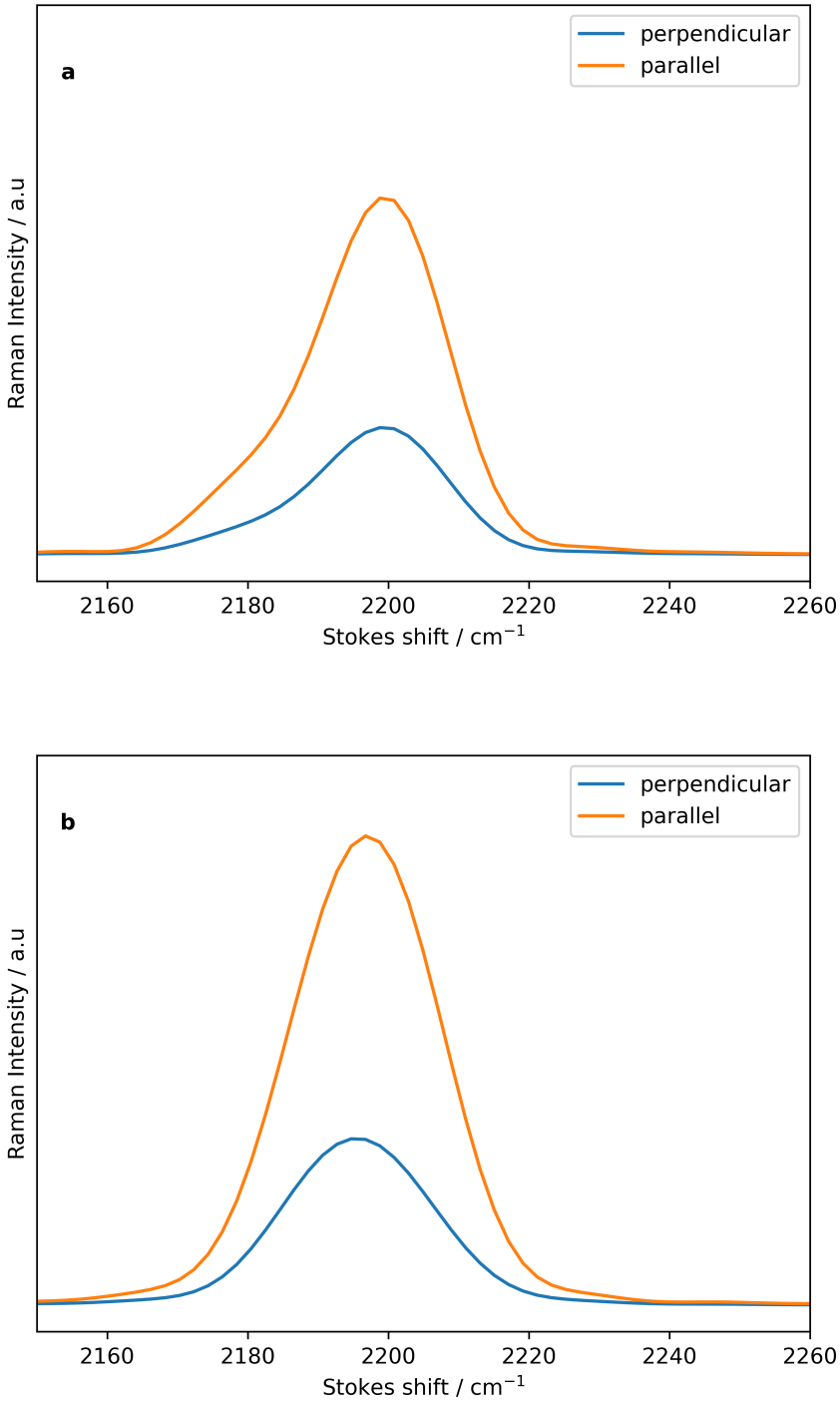

Figure 6.5: (a) C–N region of Raman spectra generated from *ab initio* molecular dynamics trajectory, at the water–vapor interface with one cyanophenol present.(b) C–N region of Raman spectra generated from *ab initio* molecular dynamics trajectory, in bulk water with one cyanophenol present.

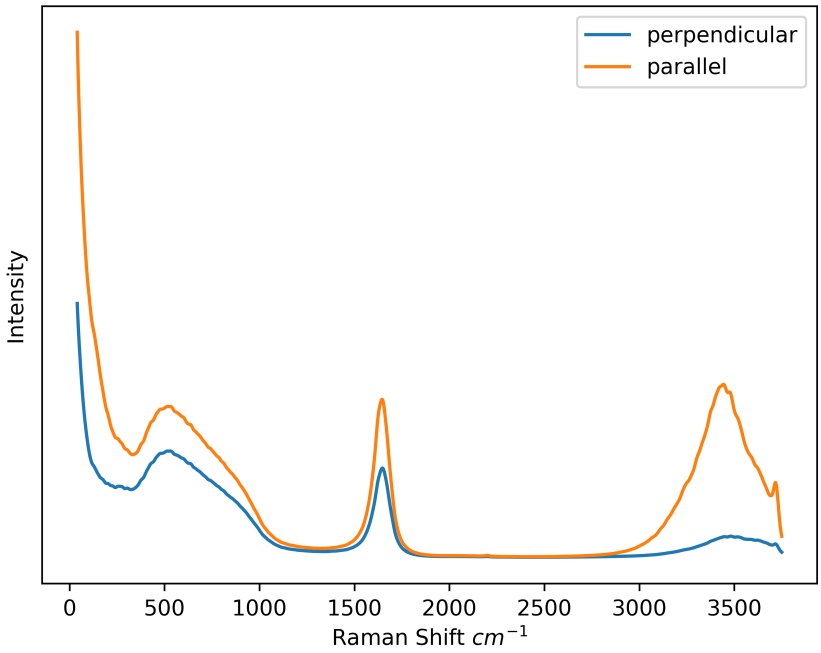

Figure 6.6: Water isolated Raman spectra generated from *ab initio* molecular dynamics trajectory at the water–vapor interface where the cyanophenol contribution has been removed.

same way; a few liquids could work for such a purpose, carbon tetrachloride is an obvious choice due to it having been used in the experimental procedure; but potentially acetonitrile could be a better choice due to it also having a cyano stretch.

6.5 Other spectra generated from *ab initio* molecular dynamics

For benchmarking purposes we have also generated power and infrared absorbance spectra in Fig. 6.9 and Fig. 6.8 respectively. These spectra are calculated in an analogous way to to Eq. 6.5 from our *ab initio* molecular dynamics trajectory; however, the infrared spectrum uses a dipole autocorrelation, while the power spectrum uses a velocity autocorrelation. We see the dominance of water-based vibrational modes in both the IR and power spectra respectively; this is due to the concentration differences between the water and the

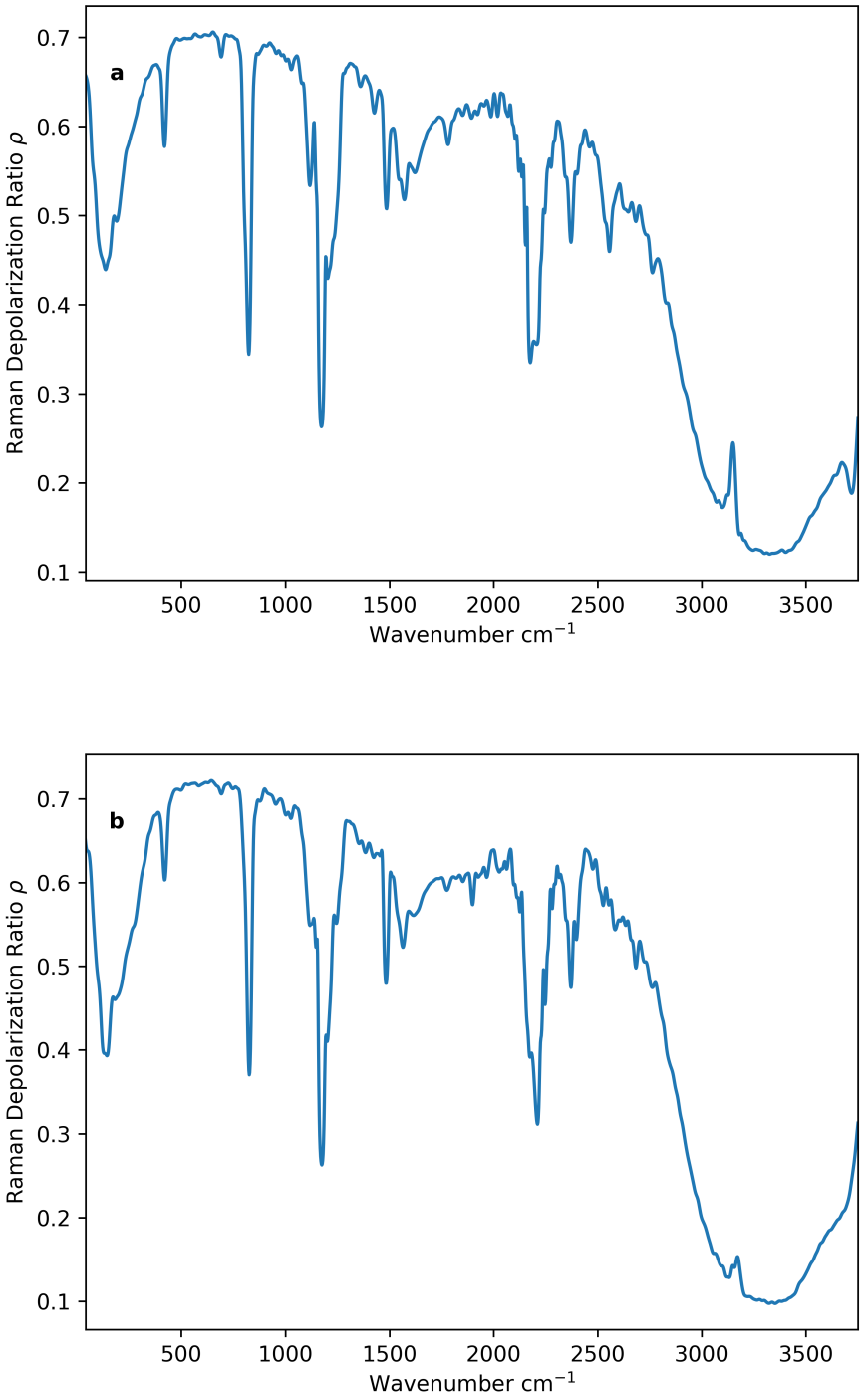

Figure 6.7: (a) Depolarization Ratio from a *ab initio* generated Raman spectra, at the water–vapor interface. (b) Depolarization Ratio from a *ab initio* generated Raman spectra, in bulk solution.

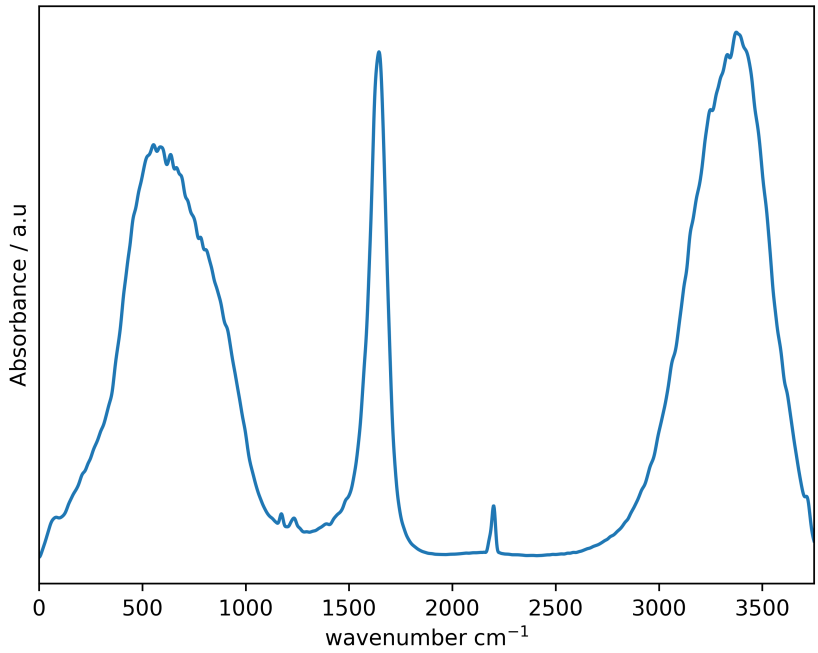

Figure 6.8: Infrared absorbance spectra generated from an *ab initio* molecular dynamics trajectory at the water–vapor interface.

cyanophenol solute.

6.6 Conclusion

From *ab initio* molecular dynamics we generated Raman spectra from interfacial and completely solvated cyanophenol. We found the depolarization ratio to vary little between the water–vapor interface and bulk solution; implying the hyperpolarizibility likely does not vary between these two modalities. We also confirmed the discovery of asymmetric broadening in the C–N mode in both bulk and surface *ab initio* spectra; whereas its origin remains a topic for further research.

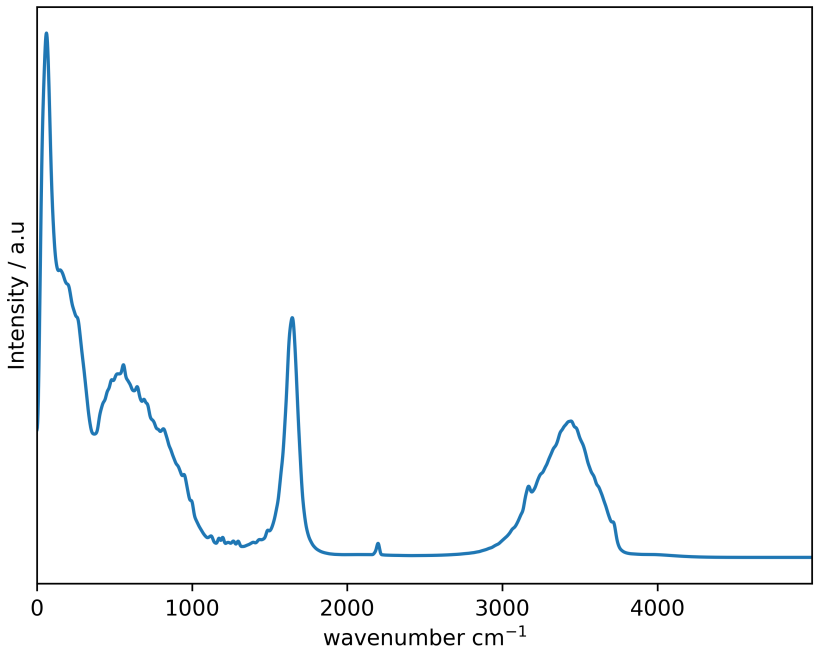

Figure 6.9: Power spectra generated from an *ab initio* molecular dynamics trajectory at the water–vapor interface.

Chapter 7

Conclusions

7.1 Summary of work

Orientational analysis of p-cyanophenol tilt, and roll angle distributions were calculated from classical molecular dynamics trajectories. The depth dependence of $\boldsymbol{\chi}^{(2)}_{\text{eff}}$ was found to be required in order to match simulation results and experimental data; the depth dependence of n' was calculated using the Lorentz-Lorenz volume fraction mixing model, while the volume fractions were calculated from a classical molecular dynamics trajectory. A 10 bin model was found to be sufficient in order to describe the depth dependence of $\boldsymbol{\chi}^{(2)}_{\text{eff}}$ based on fitting to experimental PPP spectra. We discovered the orientational relationship $\langle\cos\theta\rangle = 3\langle\cos^3\theta\rangle$, this allows for the separation of the hyperpolarizibility from the PPP data, which allowed for the study of the interfacial refractive index. We also found the requirement of an organic component to n' in order to assure proper fit to the experimental data.

Generalized symmetrical linear relationships between elements of $\boldsymbol{\chi}^{(2)}_{\text{eff}}$ were derived, and their implications on measurement of the orientational distribution were discussed. From fitting experimental data with a Faddeeva function, R was found to be within a range of 0.13 ± 0.03. A new relationship between the hyperpolarizability ratio and polarizer angles in a polarizaion null angle experiment was derived. *Ab initio* molecular dynamics simulations were performed in order to generate interfacial and bulk-phase Raman spectra in order to probe anisotropy of the depolarization ratio; where it was found that the bulk

depolarization ratio was representative of the interfacial environment. By analysing the shape of the C–N mode in *ab initio* and experimental spectra we found peculiar asymmetric broadening.

7.2 Future work

From this thesis, quite a few remaining topics of computational and experimental interest remain. To begin, a polarization null angle measurement would be of great interest, as the removal of the need for the calibration of the data would greatly simplify the analysis; while benefits inherent to PNA such as less experimental error would be of great assistance. A heterodyne SFG measurement would also allow for the inspection of the imaginary spectrum, where the asymmetric broadening could continue to be studied. With access to higher resolution SFG measurements, we could also similarly study the asymmetric broadening, and potentially narrow our range of possibilities for the hyperpolarizibility ratio. Another measurement of interest could be to analyse another isomer of cyanophenol such as meta or ortho cyanophenol. Because of the differences in relative C–N bond location one might expect stronger SFG signal due to stronger ordering; given that we can assume the hyperpolarizibility ratio to be the same among these molecules possibly even a direct measurement of the interfacial refractive index is possible.

Computationally, we could simulate each layer of water by labeling atoms in an *ab initio* molecular dynamics trajectory which would allow for a depth dependant measurement of liquid-vapor interface, or more interestingly charged interfaces with the possibility of adding ionic contributions to the solution. The *ab initio* molecular dynamics simulations could also be aided by changing the probing time-step of the electron density; while simultaneously investigating other combinations of functionals or basis sets. Improving the orientation distribution from the *ab initio* molecular dynamics trajectory (for example by probing snapshots of the classical trajectory) would allow for the calculation of accurate SFG spectra; then the interfacial refractive index could also be studied.This could

be done in a few ways; firstly by direct comparison with experimental data, as the *ab initio* SFG spectra have no local field correction. Alternatively one could directly calculate n' from the simulated $\boldsymbol{\chi}^{(1)}$ response.

References

[1] Pratt, L. R.; Pohorille, A. *Chem. Rev.* **2002,** *102,* 2671–2692.

[2] Somorjai, G. A.; Li, Y. *Proc. Nat. Acad. Sci. USA* **2011,** *108*, 917–924.

[3] Kusaka, R.; S.Nihonyanagi,; Tahara, T. *Nat. Chem.* **2021,** *13*, 306–311.

[4] Björneholm, O.; Hansen, M. H.; Hodgson, A.; Liu, L.-M.; Limmer, D. T.; Michaelides, A.; Pedevilla, P.; Rossmeisl, J.; Shen, H.; Tocci, G.; Tyrode, E.; Walz, M.-M.; Werner, J.; Bluhm, H. *Chem. Rev.* **2016,** *116,* 7698–7726.

[5] Boyd, R. W. *Nonlinear Optics;* Academic Press: San Diego, 4nd ed.; 2020.

[6] Morita, A. *Theory of Sum Frequency Generation Spectroscopy;* Springer: Singapore, 2018.

[7] Shen, Y. R. *Fundamentals of Sum-Frequency Spectroscopy;* Cambridge University Press: Cambridge, 2016.

[8] Shen, Y. R. *The Principles of Nonlinear Optics;* John Wiley & Sons: New York, 1984.

[9] Wang, H.-F.; Gan, W.; Lu, R.; Rao, Y.; Wu, B. H. *Int. Rev. Phys. Chem.* **2005,** *24,* 191–256.

[10] Wang, H.-F.; Velarde, L.; Gan, W.; Fu, L. *Annu. Rev. Phys. Chem.* **2015,** *66,* 189–216.

[11] Allen, M. P.; Tidesley, D. J. *Computer Simulation of Liquids;* Oxford University Press: Oxford UK, 2017.

[12] Unke, O. T.; Chmiela, S.; Sauceda, H. E.; Gastegger, M.; Poltavsky, I.; Schütt, K. T.; Tkatchenko, A.; Müller, K.-R. *Chem. Rev.* **2021,** *121,* 10142–10186.

[13] Becker, C. A.; Tavazza, F.; Trautt, Z. T.; Buarque de Macedo, R. A. *Curr. Op. Sol. State Mater. Sci.* **2013,** *17,* 277–283.

[14] Tarasova, E.; Nerukh, D. *J. Phys. Chem. Lett.* **2018,** *9,* 5805–5809.

[15] van der Spoel, D.; Lindahl, E.; Hess, B.; Groenhof, G.; Mark, A. E.; Berendsen, H. J. C. *J. Comp. Chem.* **2005,** *26,* 1701–1718.

[16] Jorgensen, W. L.; Tirado-Rives, J. *Jour. Am. Chem. Soc* **1987,** *110,* 1657–1666.

[17] Jorgensen, W.; Chandrasekhar, J.; Madura, J.; Impey, R.; Klein, M. *J. Chem. Phys.* **1983,** *79,* 926–935.

[18] Jorgensen, W. L.; Tirado-Rives, J. *Proc. Nat. Acad. Sci. USA* **2005,** *102,* 6665–6670.

[19] Dodda, L. S.; Vilseck, J. Z.; Tirado-Rives, J.; Jorgensen, W. L. *J. Phys. Chem. B* **2017,** *121,* 3864–3870.

[20] Dodda, L. S.; Cabeza de Vaca, I.; Tirado-Rives, J.; Jorgensen, W. L. *Nucleic Acids Res.* **2017,** *45,* W331–W336.

[21] Soule, M. C. K.; Hore, D. K.; Fellin, D. M. J.; Richmond, G. R. *J. Phys. Chem. B* **2006,** *110,* 16575–16583.

[22] Hoover, W. G.; Holian, B. L. *Phys. Lett. A* **1996,** *211,* 253–257.

[23] Parrinello, M.; Rahman, A. *J. Appl. Phys.* **1981,** *52,* 7182–7190.

[24] Becke, A. D. *J. Chem. Phys.* **1993,** *98,* 5648–5652.

[25] Becke, A. D. *Phys. Rev. A* **1988,** *38,* 3098–3100.

[26] Kendall, R. A.; Dunning, T. H., J.; Harrison, R. J. *J. Chem. Phys.* **1992,** *96,* 6796–6806.

[27] Frisch, M. J. *et al.* "Gaussian 16 Revision C.01", 2016 Gaussian Inc. Wallingford CT.

[28] Kumarasiri, A.; Yang, P.; Hore, D. K. *J. Phys. Chem. Lett.* **2023,** *14,* 4449–4453.

[29] Hale, G. M.; Querry, M. R. *Appl. Opt.* **1973,** *12,* 555–563.

[30] Kühne, T. D. *et al. J. Chem. Phys.* **2020,** *152,* 194103.

[31] Lippert, G.; Hutter, J.; Parrinello, M. *Mol. Phys.* **1997,** *92,* 477–488.

[32] Luber, S.; Iannuzzi, M.; Hutter, J. *J. Chem. Phys.* **2014,** *141,* 094503.

[33] Thomas, M.; Brehm, M.; Kirchner, B. *Phys. Chem. Chem. Phys.* **2015,** *17,* 3207–3213.

[34] Brehm, M.; Thomas, M.; Gehrke, S.; Kirchner, B. *J. Chem. Phys.* **2020,** *152,* 164105.

[35] Brehm, M.; Kirchner, B. *J. Chem. Inf. Model.* **2011,** *51,* 2007–2023.

[36] Zhuang, X.; Miranda, P. B.; Kim, D.; Shen, Y. R. *Phys. Rev. B* **1999,** *59,* 12632-12640.

[37] Guyot-Sionnest, P.; Hunt, J. H.; Shen, Y. R. *Phys. Rev. Lett.* **1987,** *59,* 1597–1600.

[38] Hall, S. A.; Jena, K. C.; Covert, P. A.; Roy, S.; Trudeau, T. G.; Hore, D. K. *J. Phys. Chem. B* **2014,** *118,* 5617–5636.

[39] Simpson, G. J.; Rowlen, K. L. *J. Am. Chem. Soc.* **1999,** *121,* 2635–2636.

[40] Roy, S.; Hung, K.-K.; Stege, U.; Hore, D. K. *Appl. Spectrosc. Rev.* **2014,** *49,* 233–248.

[41] Dang, L.; Feller, D. *J. Phys. Chem. B* **2000,** *104,* 4403–4407.

[42] Zheng, D.-S.; Wang, Y.; Liu, A.-A.; Wang, H.-F. *Int. Rev. Phys. Chem.* **2008,** *27,* 629–664.

[43] Ekhoff, J. A.; Rowlen, K. L. *Anal. Chem.* **2002,** *74,* 5954–5959.

[44] Teschke, O.; Ceotto, G.; de Souza, E. F. *Phys. Rev. E* **2001,** *64,* 011605.

[45] Bonthuis, D. J.; Gekle, S.; Netz, R. R. *Phys. Rev. Lett.* **2011,** *107,* 166102.

[46] Shiratori, K.; Morita, A. *J. Chem. Phys.* **2011,** *134,* 234705.

[47] Chiang, K. Y.; Seki, T.; Yu, C. C.; Ohto, T.; Hunger, J.; Bonn, M.; Nagata, Y. *Proc. Nat. Acad. Sci. USA* **2022,** *119,* e2204156119.

[48] Yu, X.; Chiang, K.-Y.; Yu, C.-C.; Bonn, M.; Nagata, Y. *J. Chem. Phys.* **2023,** *158,* 044701.

[49] Yu, C. C.; Seki, T.; Wang, Y.; Bonn, M.; Nagata, Y. *Phys. Rev. Lett.* **2022,** *128,* 226001.

[50] Yu, C. C.; Seki, T.; Chiang, K. Y.; Tang, F.; Sun, S.; Bonn, M.; Nagata, Y. *J. Phys. Chem. B* **2022,** *126,* 6113–6124.

[51] Born, M.; Wolf, E. *Principles of Optics;* Pergamon Press Ltd.: Oxford, 4th ed.; 1970.

[52] Murata, R.; Inoue, K.-i.; Wang, L.; Ye, S.; Morita, A. *J. Phys. Chem. B* **2021,** *125,* 9794–9803.

[53] Wan, L.; Murata, R.; Inoue, K.; Ye, S.; Morita, A. *J. Phys. Chem. B* **2021,** *125,* 9804–9810.

[54] Wang, L.; Murata, R.; Snoue, K.; Ye, S.; Morita, A. *J. Phys. Chem. B* **2021,** *126,* 2143.

[55] Wang, L.; Nihonyanagi, S.; Inoue, K.-i.; Nishikawa, K.; Morita, A.; Ye, S.; Tahara, T. *J. Phys. Chem. C* **2019,** *123,* 15665–15673.

[56] Roy, S.; Post, J. S.; Hung, K.-K.; Stege, U.; Hore, D. K. *J. Mol. Struct.* **2014,** *1069,* 103–111.

[57] Plocinik, R. M.; Everly, R. M.; Moad, A. J.; Simpson, G. J. *Phys. Rev. B* **2005,** *72,* 125409.

[58] Simpson, G. J.; Rowlen, K. L. *Anal. Chem.* **2000,** *72,* 3399–3406.

[59] Simpson, G. J.; Rowlen, K. L. *Anal. Chem.* **2000,** *72,* 3407–3411.

[60] Lu, R.; Gan, W.; Wang, H. *Chin. Sci. Bull.* **2003,** *48,* 2183–2187.

[61] Rao, Y.; Tao, Y.-S.; Wang, H. *J. Chem. Phys.* **2003,** *119,* 5226–5236.

[62] Sovago, M.; Vartiainen, E.; Bonn, M. *J. Phys. Chem. C* **2009,** *113,* 6100–6106.

[63] Yakovenko, S. Y.; Maiwald, M.; Würflinger, A.; Pelzl, J. *J. Liq. Cryst.* **1999,** *26,* 23–30.

[64] Dalmolen, L. G. P.; de Leu, W. H. *J. Chem. Phys.* **1983,** *78,* 7353–7361.

[65] Miyano, K. *J. Chem. Phys.* **1978,** *69,* 4807–4813.

[66] Saito, K.; Peng, Q.; Qiao, L.; Wang, L.; Joutsuka, T.; Ishiyama, T.; Ye, S.; Morita, A. *Phys. Chem. Chem. Phys.* **2017,** *19,* 8941–8961.

[67] Hore, D. K.; Beaman, D. K.; Parks, D. H.; Richmond, G. L. *J. Phys. Chem. B* **2005,** *109,* 16846–16851.

[68] Choi, J.; Kwansa, A. L.; Yingling, Y. G.; Kim, S. H. *J. Phys. Chem. B* **2023,** *127,* 8456–8467.

[69] Chase, H. M.; Rudshteyn, B.; Psciuk, B. T.; Upshur, M. A.; Strick, B. F.; Thomson, R. J.; Batista, V. S.; Geiger, F. M. *J. Phys. Chem. B* **2016,** *120,* 1919–1927.

[70] Placzek, G. Handbuch der Radiologie. In ; Akademische Verlagsgesellschaft: Leipzig, 1934.

[71] Zhang, D.; Gutow, J.; Eisenthal, K. B. *J. Phys. Chem.* **1994,** *98,* 13729–13734.

[72] Thomas, M.; Brehm, M.; Fligg, R.; Voehringer, P.; Kirchner, B. *PCCP* **2013,** *15,* 6608–6622.

[73] Fischer, S. A.; Ueltschi, T. W.; El-Khoury, P. Z.; Mifflin, A. L.; Hess, W. P.; Wang, H.-F.; Cramer, C. J.; Govind, N. *J. Phys. Chem. B* **2016,** *120,* 1429–1436.